Novel Turbulence Model Tailored For Complex Rocket Motor Exhaust Jets

Robert E. Childs * and Kristen V. Matsuno †
NASA Ames Research Center, Moffett Field, CA 94035

This paper describes a new RANS turbulence model intended to give improved accuracy in turbulence that is affected by compressibility, rotation and curvature, and variable density, making it well-suited to complex rocket motor exhaust jets. Four key elements of the model are: the use of simple-averaged (not mass-averaged) turbulence decomposition; a second-order Taylor series for the equilibrated turbulent fluxes; empirical modeling that accounts for the combined effects of aforementioned turbulence modifiers; and model tuning on large-eddy simulation data for mixing layers for a wide range of these turbulence modifiers. The model is implemented as an extension of the k-ω SST model. Results include comparisons to detached-eddy simulation results for hot and cold co-flowing exhaust jets, and to experimental data for supersonic retropropulsion on the CobraMRV Mars-lander concept vehicle. The model is named TMRC for its constituents elements, the Taylor series with Mach number, rotation and curvature effects.

I. Introduction

On many launch vehicles, the rocket motor exhaust jets typically interact weakly with the vehicle's external aerodynamics, so turbulence modeling in these plumes has limited impact on the vehicle's aerodynamic characteristics. In applications like supersonic retro-propulstion (SRP) and on the Orion Launch Abort Vehicle (LAV), the plumes can have a very strong effect on vehicle aerodynamics, and the ability to accurately predict the plumes' behavior is critical. NASA has observed that turbulence modeling and chemical reactions are two dominant source of inaccuracy or uncertainty in CFD simulations of these types of flows. By implication, chemically reacting rocket plumes may be needed in physical simulations. Wind tunnel experiments have traditionally been used to characterize complex vehicle aerodynamics, but the inclusion of reacting flows makes wind tunnel testing more challenging and expensive. As a result, the LAV's aerodynamic database relies heavily on reacting-flow CFD results. Design of SRP systems for landing on Mars is further complicated by the need to approximate the planet's tenuous atmosphere of mostly CO_2. These factors would make CFD a more attractive means of characterizing the aerodynamics of entry, descent and lander vehicles that employ retro-propulsion, but good CFD accuracy for SRP flows remains elusive. This work addresses turbulence modeling suitable for these types of energetic jets, in the absence of chemical reactions, but including the effects of high temperatures.

Several flow phenomena relevant to rocket plume turbulence and its modeling are summarized here. (1) The jets' gross features are set by the inviscid shock-cell pattern, with barrel shocks and compressions that have alternating signs of the streamline curvature. (2) The surrounding plume shear layer experience rotation and curvature (RC) effects of alternating sign, which are further affected by temperature and density gradients. (3) Classical compressible (CC) effects occur at the high convective Mach number, M_c, across the plume shear layer. (4) Flow through shocks does not inherently generate significant turbulence, but can do so under many conditions. (5) Mach disks are normal shocks that can appear in the core of a jet and reduce the length of a shock cell; they create pockets of high-temperature low-subsonic 'wake flow' with a surrounding shear layer at high M_c. (6) In a jet inclined to the freestream, the main shear-layer vorticity rolls up into a pair of counter-rotating vortices. (7) Interactions among these effects are suspected; M_c-RC interactions are characterized and modeled in this work.

The TMRC model consists of several modifications to the SST model[1, 2] which are intended to improve modeling fidelity for the turbulence mechanisms that are active in rocket exhaust plumes. The 'stock' forms of engineering-level turbulence model such as SA, k-ω, SST and k-ϵ do not model critical core behaviors like CC and RC effects with good accuracy, and numerous model modifications have been proposed to improve modeling accuracy. Many experiments and modeling development efforts have focused on individual effects, such as CC effects in planar shear layers, and RC

*Senior Research Scientist, Science and Technology Corp, Hampton VA
†Aerospace Engineer, NASA Systems Analysis Office, AIAA Member

effects at low Mach numbers. Overflow's implementation of the SST model includes the Suzen[3] CC option and the RC option from the SA-RC model[4, 5]. It would seem logical to enable these two options for rocket plumes, but doing so generally gave inferior results for overall plume characteristics and the loads on the Orion LAV, relative to using the unaltered stock SST model[6]. This work seeks to remedy this sort of unacceptably poor accuracy, from enabling model options that ought to improve accuracy. The Taylor-series part of the TMRC model is mathematically general and applicable to all low-speed flows. The full TMRC model explicitly addresses modeling of combined CC and RC effects. The modeling described here and the predecessor to this work, the SST-MRC model[6], include an interaction in which CC effects are diminished by unstable RC effects. Section II describes this and other feature of the TMRC model. LES and DES (large/detatched eddy simulation) of relevant model problems, given in Section III, were used to generate data that were used to tune the TMRC model and assess its accuracy.

The turbulence in SRP rocket plumes involves all of the phenomena noted above, and several other important flow characteristics, which have typically been observed in wind tunnel experiments. (1) Unsteadiness occurs at low frequencies and length scales large enough to span all of a jet's extent. Some of the flow fluctuations presented below may be described as 'potential' rather than 'vortical' turbulence, so a statistic like $\overline{\omega_i'\omega_j'}$ is better than $\overline{u_i'u_j'}$ at identifying true turbulence. (2) As a result of large scale turbulence, the bow shock is dynamically deformed and sheds large-scale fluctuations in vorticity and entropy, which then feed into turbulence at those scales. Dynamical shocks occur throughout SRP flows. (3) The freestream and rocket plumes are in roughly opposite directions, and multiple 'floating stagnation points' may exist which are prone to instability. (4) The path for a feedback mechanism exists in form of disturbance propagating outward on the jets, and convecting back to the vehicle on the very disrupted freestream flow. The aggregate effect of this unsteadiness is not amenable to steady RANS turbulence modeling.

It is likely that good accuracy for SRP flows will only be achieved with simulation methods that resolve some fraction of the jet-plume turbulence, but it is unknown whether URANS may suffice or if methods akin to DES modeling will be required. Despite the expectation that DES methods would be superior to RANS for SRP, the initial Overflow work focused exclusively on URANS simulations with the SST turbulence model. Of the three CFD solvers in this group of companion papers[7–9], Overflow, FUN3D and LociChem, Overflow had routinely given plausible results using SST, and it was the logical choice for this work. The FUN3D and LociChem efforts used turbulence modeling that gave unsteady DES-like results.

When the relatively poor accuracy of SST modeling was observed at high SRP thrust coefficients, the Overflow simulations of the CobraMRV were expanded to include the DES and the TMRC model. The rationale for evaluating the TMRC model on SRP flows was to determine if the poor accuracy of the SST-URANS results was principally due to the SST model, which would be altered by the TMRC model, or if RANS models in general are inherently unable to function well in SRP flows. Results given below demonstrate that the TMRC model can give steady or unsteady results, depending on the nature of the mean flow. Simple forward-flowing mixing layers and jets tend to be steady, but flows with 'bluff-base' wakes are often unsteady. A jet in crossflow has characteristics of a bluff-base flow such as Strouhal shedding, and TMRC simulations of SRP flows are generally unsteady. Thus, the TMRC model may be able to predict some flow characteristics that are associated with large-scale SRP unsteadiness, while also giving better accuracy than the stock SST model for key elements of 'simple' rocket plumes that were listed above. Comparisons of DES and TMRC simulations and experiment for SRP on the CobraMRV are given by Matsuno[8] and in Section IV.

II. Model Development

This section describes the TMRC model, which consists of the theoretical Taylor series elements and the empirical M_c-RC modeling. The Taylor-series concept is a new approach to deriving turbulence model equations, and it leads to an Algebraic Stress Modeling (ASM) for the turbulent fluxes (mass-flux vector, stress tensor). The MRC part of the model involves modeling of CC effects due to elevated M_c, and their interaction with RC effects.

A. Physics Equations

The work starts by defining the underlying physics model of fluid dynamics and the decomposition of that physics into mean and fluctuations. Field models and Lagrangian particle (LP, "atomic") models are both well-suited to deriving equations of turbulence. The two describe physics that is inherently similar for convective processes, but certain tasks are better handled by atomic theory. Atomic theory has been used to address aspects of RC modeling and isentropic compressible fluctuations. The primary description herein is the conventional 'field-equation' form. The analysis presented here is based on simple-averaged turbulence decomposition for velocity ($u_i = \overline{u}_i + u_i'$) and for density ($\rho = \overline{\rho} + \rho'$). The analysis also switches fluidly between density and its reciprocal, the specific volume

$(1/\rho = \nu = \overline{\nu} + \nu')$. A series expansion truncated at first order in ρ' gives $\nu'/\nu = -\rho'/\rho$. The starting point for the evolution equations for incompressible variable-density turbulence consists of the density / specific volume and momentum conservation equations,

$$\dot{\rho} = 0, \qquad \dot{\nu} = 0, \qquad \dot{u}_i = \nu P_i + g_i, \qquad \dot{\rho u}_i = P_i + \rho g_i \tag{1}$$

in which the 'dot' notation is the Lagrangian time derivative. Tensor notation is used for field-variable gradients such as $P_i = \partial p/\partial x_i$, $D_i = \partial \rho/\partial x_i$ and $U_{ij} = \partial u_i/\partial x_j$; strain and rotation rate tensors are S_{ij} and R_{ij}. The conventional notation for mass-averaged velocities, $\tilde{u}_i = \overline{\rho u_i}/\overline{\rho}$, is retained.

This work uses the density/volume and velocity-form ($\dot{u}_i$) of the momentum equation. In prior model development work, a large difference in accuracy for hot and cold jets was observed. Thus, a primary concern is to capture the effects of temperature/density gradients and density fluctuations, which both emerge from the turbulence decomposition of the product νP_i. The momentum-form ($\dot{\rho u}_i$) captures the turbulent density interactions with gravity g_i, but not with the pressure gradient.

B. Taylor Series for Turbulent Stress Tensor

The mathematical basis of this work is a second-order temporal Taylor series for the turbulent stress tensor τ_{ij}, and the assumption that its asymptotic state is reached after an 'equilibration time interval' Δt, on a trajectory set by the semi-exact production terms. This Δt is initially a physical time interval, and the Taylor series describes the evolution of τ_{ij} from from an initial time t_0 to a later time $t_0 + \Delta t$. The ASM model assumption is to integrate this time evolution analytically, so τ_{ij} is always at its equilibrated state $\tau_{ij}[t_0 + \Delta t]$. At this point, Δt has lost its original connection to physical time, and becomes a model-assumption equilibration time interval. The physical time is t_0, and the Taylor series for the equilibrated stress tensor is

$$\tau_{ij}[t_0 + \Delta t] = \underbrace{\tau_{ij}[t_0]}_{\text{ICs}} + \Delta t \underbrace{\dot{\tau}_{ij}[t_0]}_{\text{RSTEs}} + \tfrac{1}{2}\Delta t^2 \underbrace{\ddot{\tau}_{ij}[t_0]}_{\text{RS}\dot{\text{T}}\text{Es}} + O(\Delta t^3) \tag{2}$$

All *rhs* terms are evaluated at the assumed initial condition of isotropic turbulence, $\tau_{ij} = \frac{2}{3}\delta_{ij}k$. The *rhs* terms include the initial conditions (ICs), and the first and second temporal derivatives, which are the Reynolds-stress transport equations (RSTEs) and their time derivative (RS$\dot{\text{T}}$Es). Reynolds-stress transport models (RSTMs) are based on the RSTEs. These models retain the exact productions terms, such as $\tau_{ik}U_{jk}$, while the many un-closed terms are modeled with phenomenological approximations. The same philosophy is applied in the Taylor series part of the TMRC model. The exact production terms are retained and extended to second-order with the $\Delta t^2\, \ddot{\tau}_{ij}$ term, while the un-closed terms are treated with approximation.

Note that second-order terms in this Taylor series analysis can include stability mechanisms, which are often second-order. However, Δt is not assumed to be small, so third- and higher-order terms may be significant.

This development is based on the simple-averaged velocity, not mass-averaged, to capture the interaction of density fluctuations and pressure gradient. A natural consequence is that the turbulent mass transport is not exactly zero. The Taylor series is developed for the mass- and momentum-transport terms.

The evolution equations for the mass and momentum fluxes are

$$\begin{aligned}
\dot{\overline{\rho' u_i'}} &= -\underbrace{\overline{u_i' u_k'}\,\overline{D}_k}_{\text{grad. diff.}} - \overline{\rho' u_k'}\,\overline{U}_{ik} - \overline{\rho' \nu'}\,\overline{P}_i + \epsilon_i \\
\dot{\tau}_{ij} = \dot{\overline{u_i' u_j'}} &= -\underbrace{\overline{u_i' u_k'}\,\overline{U}_{jk} - \overline{u_j' u_k'}\,\overline{U}_{ik}}_{\text{stress-strain production}} - \underbrace{\overline{\nu' u_i'}\,\overline{P}_j - \overline{\nu' u_j'}\,\overline{P}_i}_{\text{baroclinic production}} + \epsilon_{ij}
\end{aligned} \tag{3}$$

with descriptive names appended to a few terms. The 'everything else neglected' terms, ϵ_i and ϵ_{ij}, include all of the unclosed terms and are omitted hereafter. The second derivative $\ddot{\tau}_{ij}$ is obtained via the derivative product rule, for example,

$$\begin{aligned}
\dot{\tau}_{ij} &= -\tau_{ik}\,\overline{U}_{jk} - \tau_{jk}\,\overline{U}_{ik} \\
\ddot{\tau}_{ij} &= -\dot{\tau}_{ik}\,\overline{U}_{jk} - \dot{\tau}_{jk}\,\overline{U}_{ik} - \tau_{ik}\,\dot{\overline{U}}_{jk} - \tau_{jk}\,\dot{\overline{U}}_{ik} \\
&= \left(\tau_{il}\,\overline{U}_{kl} + \tau_{kl}\,\overline{U}_{il}\right)\overline{U}_{jk} + \left(\tau_{jl}\,\overline{U}_{kl} + \tau_{kl}\,\overline{U}_{jl}\right)\overline{U}_{ik} - \tau_{ik}\,\dot{\overline{U}}_{jk} - \tau_{jk}\,\dot{\overline{U}}_{ik}
\end{aligned} \tag{4}$$

The second derivative used in the Taylor series is initially developed with all exact production terms retained up to second order. The process outlined above is used to make the full Taylor series equations for the mass and momentum fluxes. The *rhs* terms are evaluated at t_0, but that notation is omitted.

$$\begin{aligned}\overline{\rho' u_i'}[t_0+\Delta t] = \overline{\rho' u_i'} - \Delta t \left(\overline{\rho' u_k'}\,\overline{U}_{ik} + \tau_{ik}\,\overline{D}_k + \overline{\nu'\rho'}\,\overline{P}_i\right) \\ + \tfrac{1}{2}\Delta t^2\Big(\big(\overline{\rho' u_l'}\,\overline{U}_{kl} + \tau_{kl}\,\overline{D}_l + \overline{\nu'\rho'}\,\overline{P}_k\big)\,\overline{U}_{ik} \\ + \big(\tau_{kl}\,\overline{U}_{il} + \tau_{il}\,\overline{U}_{kl} + \overline{\nu' u_k'}\,\overline{P}_i + \overline{\nu' u_i'}\,\overline{P}_k\big)\,\overline{D}_k + 2\overline{\nu' u_k'}\,\overline{D}_k\,\overline{P}_i\Big)\end{aligned} \tag{5}$$

and

$$\begin{aligned}\tau_{ij}[t_0+\Delta t] = \tau_{ij} + \Delta t\,\big(-\tau_{ik}\,\overline{U}_{jk} - \tau_{jk}\,\overline{U}_{ik} + \overline{\nu' u_i'}\,\overline{P}_j - \overline{\nu' u_j'}\,\overline{P}_i\big) \\ + \tfrac{1}{2}\Delta t^2\Big(\big(\tau_{il}\,\overline{U}_{kl} + \tau_{kl}\,\overline{U}_{il} + \overline{\nu' u_i'}\,\overline{P}_k + \overline{\nu' u_k'}\,\overline{P}_i\big)\,\overline{U}_{jk} - \tau_{ik}\,\dot{\overline{U}}_{jk} \\ + \big(\tau_{jl}\,\overline{U}_{kl} + \tau_{kl}\,\overline{U}_{jl} + \overline{\nu' u_j'}\,\overline{P}_k + \overline{\nu' u_k'}\,\overline{P}_j\big)\,\overline{U}_{ik} - \tau_{jk}\,\dot{\overline{U}}_{ik} \\ + \big(\overline{\nu' u_k'}\,\overline{U}_{ik} - \tau_{ik}\,\overline{D}_k/\overline{\rho}^2 - \overline{\nu'\nu'}\,\overline{P}_i\big)\,\overline{P}_j \\ + \big(\overline{\nu' u_k'}\,\overline{U}_{jk} - \tau_{jk}\,\overline{D}_k/\overline{\rho}^2 - \overline{\nu'\nu'}\,\overline{P}_j\big)\,\overline{P}_i\Big)\end{aligned} \tag{6}$$

This form of the Taylor series retains all terms and its derivation is obvious. Model development is based on a reduced form of these equations. Tensor symmetry rules are used where applicable, such as converting $U_{ik}U_{jk}$ to products of S_{ij} and R_{ij}. The Taylor series initial condition is evaluated at the assumed state of isotropic turbulence $\tau_{ij} = \frac{2}{3}\delta_{ij}k$ with $\rho' = 0$, which can be computed from the k-ω variables. Terms that are zero under these assumptions are omitted in subsequent equations. The turbulent fluxes are now given by

$$\begin{aligned}\overline{\rho' u_i'}[t_0+\Delta t] = &\quad - \;k\Delta t\;\overline{D}_i \;+\; \tfrac{1}{2}k\Delta t^2\big(\overline{U}_{ik}\,\overline{D}_k + (\overline{U}_{ik} + \overline{U}_{ki})\,\overline{D}_k\big) \\ \tau_{ij}[t_0+\Delta t] = \tfrac{2}{3}k\delta_{ij} - \tfrac{4}{3}k\Delta t\,\overline{S}_{ij} \;+\; &\tfrac{2}{3}k\Delta t^2\big((\overline{S}_{jk} + \overline{R}_{jk})\,\overline{S}_{ik} + (\overline{S}_{ik} + \overline{R}_{ik})\,\overline{S}_{jk} - \dot{\overline{S}}_{ij} - (\overline{D}_i\,\overline{P}_j + \overline{D}_j\,\overline{P}_i)/\overline{\rho}^2\big)\end{aligned} \tag{7}$$

Next, approximate Δt using ω^{-1} and $|U_{ij}|^{-1}$. Assuming $\Delta t = \frac{3}{2}\omega^{-1}$ causes the first-order term to become the basic k-ω eddy-viscosity stress.

$$\tau_{ij}[t_0+\Delta t] = \tfrac{2}{3}\delta_{ij}k - 2\frac{k}{\omega}\,\overline{S}_{ij} \;+\; O(\Delta t^2) \tag{8}$$

In other words, the Taylor series predicts that an eddy-viscosity stress is *the* correct first-order approximation of the equilibrium stress tensor. Gradient diffusion is the first-order mass flux.

The ASM elements are found in the second-order terms. The two $R_{ik}S_{jk}$ terms form the core of the stress-tensor rotation process in the QCR modeling concept from Saffman[10], Knight[11], Wilcox[12], and Mani[13]. The familiar $\dot{S}_{ij}$ term of the RC mechanism in the SA-RC model appears as a mean-flow 'history' term, not a stability process which must involve feedback within the stress tensor. The baroclinic Brunt-Väisälä (BV) stability mechanism comes from the trace of the $-\overline{D}_j\,\overline{P}_i$ terms, when the body force of gravity is converted to the volumetric force of the pressure gradient. The Taylor series theory deals with time-averages, so it misses the complex physics of BV theory, and an adjustment is required in the Taylor-series-based modeling. Equation 7 contains $S_{ik}S_{jk}$ terms that have not been identified in the context of previous QCR-like modeling, so there is no prior example of how they should be used in the present effort. Work focused on higher-order tensor-invariants has presumably addressed these terms, and the Taylor series can complement that work by suggesting physical foundations for higher-order invariant methods. Using QCR as guidance, we take the second-order $\Delta t^2 = (\omega|U_{ij}|)^{-1}$. The viable velocity gradient time scale for QCR terms is $|U_{ij}|^{-1}$, as $|R_{ij}|$ or $|S_{ij}|$ can be zero when $|U_{ij}|$ is nonzero, leading to ill-conditioned behavior. Thus, the current ASM exactly replicates the stress-rotation of the QCR model[13], with a suitable choice of model coefficients. The primary time scale in the Taylor series is the all-purpose k-ω time scale $\Delta t = \omega^{-1}$, while there are secondary time scales in $|U_{ij}|^{-1}$ and the baroclinic process. The mathematical rigor of the Taylor series is compromised by casually using the most convenient time scale. However, the existing k-ω model typically predicts $\omega/|U_{ij}|$ to be roughly constant. There are also benefits of building on existing modeling experience.

There are many adjustments to the Taylor series when it is converted into a working model. Modeling guidance is obtained from RSTMs, which generally approximate the pressure-strain mechanism in terms of return-to-isotropy and anti-production processes. See, e.g., Rumsey[14] for summary of these models. The RSTM treatment of the

pressure-strain mechanisms has the net effect of diminishing the exact production terms. The logic of mimicking RSTM models is to set model coefficients on source terms in the k-ω equations to reflect those losses. In reality, the coefficients are tuned on data from LES, and that tuning is presumed to be consistent with the logic. The conventional RC stability mechanism does not appear in the field-equation form of the Taylor series, but it does emerge from the atomic form. Atomic theory is also used to convert the density gradient $\overline{D_i}$ to its isentropic form.

Some terms from the Taylor series analysis are omitted from the current form of the TMRC model. A few key omissions, and the rationale therefore, are given here. The mass flux includes only the density-gradient diffusion term, a first-order term, as this is the logical first step in treating turbulent mass transport. The second-order terms like $\overline{D_k}\,\overline{U_{ik}}$ are omitted. The baroclinic terms are not included in the momentum flux tensor, when used in the Navier-Stokes solver. They are complicated to compute, and Overflow does not currently have a means of storing the the stress tensor for later use in computing the stress-strain production of *tke* (*tke* = k and is easier to read). The increment to the stress tensor they would create is independent of the velocity gradient, so it will not promote stable behavior of the turbulence model/mean flow system. Thus, a 'stand-alone' baroclinic stability production term is included in the k-ω equations, Eqn. 11. It is required to generate *tke*, and it is tuned to match data from a baroclinic-dominated mixing layer. Mass-averaged velocity gradients are used, while the Taylor-series analysis is based on simple-averaged velocity gradients. The conservation variable in compressible flow solvers is momentum, from which mass-averaged mean velocity gradients are computed. These two gradients differ in proportion to the magnitude of density fluctuations, so this assumption is valid for small density fluctuation.

Important conceptual details have emerged from the theory. The RC mechanism consists of new source terms, not as a scale factor applied to the stress-strain production. The RC mechanism consists of separate kinematic and baroclinic parts, denoted *kRC* and *bRC*. The *kRC* part depends on the velocity field, as in typical RC models, and is independent of the density gradient. The *bRC* part depends entirely on density gradient, and its interaction with the pressure gradient which is often associated with flow on a curved path.

Thus, the Taylor series predicts several elements of turbulence modeling that are generally accepted as representing the state-of-the-art for 'production-level' aerodynamics work; these elements create a solid theoretical foundation for modeling. Some aspects of the TMRC model seek to honor the intent of the known physics, while others are just pragmatic model approximations.

C. TMRC Taylor Series Equations

The model equations as implemented in TMRC version 2023.012 are given below, and used for the CFD results presented here. A version 2024.001 exists and is being tested and refined. The equations used to compute the turbulent fluxes are

$$
\begin{aligned}
\overline{\rho' u_i'} &= -\underbrace{[1]\nu_t\,\overline{D_i}}_{\text{grad. diff.}} \\
\overline{\rho}\,\overline{u_i' u_j'} &= \underbrace{[0.0]\overline{\rho}\,k\delta_{ij}}_{\text{normal stress}} - \underbrace{2\mu_t\widetilde{S}_{ij}}_{\text{grad. diff.}} + \underbrace{[0.95](\tilde{u}_j\overline{\rho' u_i'} + \tilde{u}_i\overline{\rho' u_j'})}_{\text{mass flux} \rightarrow \text{mom. flux}} \\
&\quad + \mu_t\Big(\underbrace{[0.1]\widetilde{S}_{ik}\widetilde{S}_{jk}}_{\text{ASM tensor strain}} + \underbrace{[0.3](\widetilde{R}_{ik}\widetilde{S}_{jk} + \widetilde{R}_{jk}\widetilde{S}_{ik})}_{\text{ASM stress tensor rotation}} \Big)/|\widetilde{U}_{ij}|
\end{aligned}
\tag{9}
$$

The model coefficients associated with the TMRC part of the model are given in brackets, e.g., [0.3], and are determined by empirical tuning. Some of these coefficients are zero in version 2023.012, but the terms are retained in the equations presented here, as a new version of the model may have non-zero values. Model coefficients from SST are unchanged and are given by their conventional symbols. The coefficient blending between near-wall and outer-layer is retained in the model, but omitted in this description. The turbulent Prandtl and Schmidt (mass-transport) numbers are 1. The eddy-viscosity is computed with the conventional SST expression, but with a realizability constraint[15]. Terms associated with the classical compressibility (CC) modeling for reduced mixing at elevated M_c are omitted here and discussed below.

The k-ω evolution equations can be written simply as

$$
\begin{aligned}
\dot{\rho k} &= \mu_t\big(2\widetilde{S}_{ij}\widetilde{S}_{ij} + P_{k,bRC} + P_{k,kRC}\big) - \beta^*\rho k\omega + (\text{diff.}) \\
\dot{\rho\omega} &= 2\gamma\overline{\rho}\,\widetilde{S}_{ij}\widetilde{S}_{ij} + P_{\omega,bRC} + P_{\omega,kRC} - \beta\rho\omega^2 + (\text{diff. \& SST cross-diff.})
\end{aligned}
\tag{10}
$$

in which the new TMRC source terms are

$$
\begin{aligned}
bRC = \quad & -\frac{1}{\rho^2}\Big(\frac{\partial \overline{p}}{\partial x_i}\Big)\Big(\frac{\partial^s \overline{\rho}}{\partial x_i}\Big), \\
kRC = & -\frac{1}{\overline{\rho}\,\widetilde{U}^2}\Big(\frac{\partial \overline{p}}{\partial x_i}\Big)\Big(\frac{1}{2}\frac{\partial \widetilde{U}^2}{\partial x_i} + \frac{1}{\rho}\frac{\partial \overline{p}}{\partial x_i}\Big) \quad \text{with limiting via } \kappa = \quad \frac{1}{\overline{\rho}\,\widetilde{U}^2}\Big|\frac{\partial \overline{p}}{\partial x_i}\Big| \\
bRC^+ = (bRC + |bRC|)/2, \quad & bRC^- = (bRC - |bRC|)/2, \text{ etc.} \\
P_{k,bRC} = [4.0]bRC^+ + [0.5]bRC^-, \quad & P_{\omega,bRC} = [2.0]bRC^+ + [-5.0]bRC^- \\
P_{k,kRC} = [0.0]kRC^+ + [0.0]kRC^-, \quad & P_{\omega,kRC} = [-5.0]kRC^+ + [-5.0]kRC^-
\end{aligned}
\tag{11}
$$

The *bRC* and *kRC* terms are the raw baroclinic and kinematic RC metric (sensor) functions. The *bRC* metric is the isentropic compressible form, from atomic theory. The notation $\partial^s \rho/\partial x$ denotes a derivative at constant entropy, and accounts for basic thermodynamics, much like the gradient of potential temperature used in meteorology. The *kRC* metric is entirely from atomic theory, and it is not Galilean invariant. Both RC terms share a common form: they involve the inner product of the pressure gradient and the density or total kinematic energy ($U^2/2$ and P) gradient. The *kRC* term is independent of the density gradient; stability behavior related to the density gradient is entirely in the *bRC* term. The streamline curvature $\kappa \sim 1/R$ is used in the *kRC* term to prevent singular behavior, such as at walls. In this work, the limiter is $\kappa \leq 10$, which limits the radius of curvature to be ≥ 0.1. For the CFD work presented here, the grids have the dimension of inches, so this limiter clips streamline curvature smaller than 0.1[in]. Adjustments for different grid dimensions or physical scales may be appropriate.

The effects of *RC* terms can be distributed to both *k*-ω variables in an effort to best match known behaviors of physical turbulence and data from the LES of mixing layers in a later section. In particular, the baroclinic instability associated with hot air creates an upward acceleration that is limited only by the dissipation/mixing of the hot air. The mean-field energy available to convert to turbulence is limited by the height of the domain, such as the atmosphere. Conversely, water-surface gravity waves do not destroy fluctuation energy; the energy persists in an enclosure or radiates away in an open space. Thus, unstable *bRC* conditions can convert significant mean energy to turbulence, but stable *bRC* conditions do not destroy turbulence energy or convert it back to mean energy which would seem to violate entropy considerations. Stable and unstable RC conditions have this fundamental difference, which is also present in the complex behavior predicted by Brunt-Väisälä theory. All of the *kRC* source terms are currently channeled through the ω equation, and hence directly affect anisotropy but not energy. The increased anisotropy multiplying the strain gives elevated production of *tke*.

D. TMRC: Mach, Rotation & Curvature Modeling

The second major part of the TMRC model deals with the general trend toward reduced turbulence in mixing layers at elevated convective Mach number M_c. This classical compressibility (CC) effect is widely recognized, but there are also significant differences in the reduction of the mixing layer growth rate with M_c from different experiments[16]. Multiple explanations for the reduced turbulence have been proposed, and multiple physical mechanisms are likely to be important. An important mechanism is the efficient Kelvin-Helmholtz (KH) growth and pairing of spanwise vortices in low-speed mixing layers, which is suppressed at elevated M_c, for the same fundamental reasons that swept wings are preferred for transonic flight. Rocket exhaust jets often have barrel-shaped shear layers that involve both RC and CC effects, and the potential for interaction between them. Specifically, the turbulence created by unstable RC effects may be resistant to stabilizing CC effects, as proposed in [6]. The streamwise Görtler vortices in wall-bounded RC-unstable flow should be unaffected by the CC mechanism that suppresses KH vortex dynamics. While Görtler vortices are generally not observed in RC-unstable mixing layers, the RC mechanism that creates them and enhances mixing is independent of the KH instability mechanism and thus not suppressed by CC effects in a similar manner. LES results in the next section demonstrate that elevated M_c has diminished effects in RC unstable mixing layers.

The basis for CC modeling is the Suzen and Hoffmann model[3], which adds dilatation-dissipation source terms to the *k*-ω equations. Using their original notation, the additonal source terms are

$$
\begin{aligned}
\dot{\rho k} \; += \; & -\rho\omega\beta^* k\alpha_1(1-F_1)M_t^2 + (-\alpha_2 P_k + \alpha_3\rho\epsilon)\,(1-F_1)M_t^2 \\
\dot{\rho\epsilon} \; += \; & \quad \beta^*\alpha_1\rho\omega^2(1-F_1)M_t^2
\end{aligned}
\tag{12}
$$

in which $M_t^2 = 2k/a^2$ is Mach number of the turbulent velocity fluctuations, P_k is the convention stress-strain production of *tke*, F_1 is the SST wall-proximity function, and the $\alpha_1, \alpha_2, \alpha_3$ and β^* are model coefficients. The M-RC part of the

TMRC model replaces the prior wall-proximity and M_t^2 effects as follows

$$(1 - F_1)M_t^2 \;\rightarrow\; (1 - F_1)^2\, F_M(M_t)\, F_{MRC}(RC) \tag{13}$$

in which $F_M(M_t)$ provides the CC modeling suitable for planar layers and is given in Fig. 1, and $F_{MRC}(RC)$ modifies the basic CC modeling to account for destabilizing RC effects and is given in Eqn. 14. Both empirical functions are tailored to match LES results for mixing layers, presented in the Section III. The original Suzen model model tends to generate an excessive CC effect in boundary layers, so that wall-proximity effect was squared.

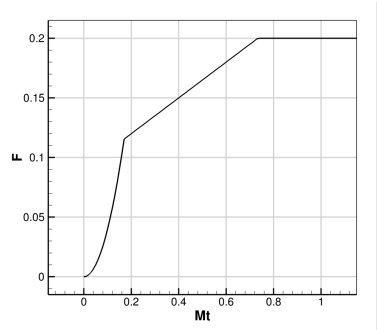

Fig. 1 Empirical function $F_M(M_t)$ that replaces M_t^2 in Suzen and Hoffmann model. F_M is constant for $M_t > 1$.

The function F_{MRC} is given by

$$\begin{aligned} F_{MRC} &= \max\big(1 - [13.0]\frac{g^+}{g^+ + S^2},\, [0.1]\big) \qquad \text{in which} \\ g &= [0.6]bRC^+ + [1.0]bRC^- + [1.0]kRC, \quad g^+ = (g + |g|)/2 \end{aligned} \tag{14}$$

The intermediate term g is a weighted sum of RC terms. The M-RC interaction is designed to become significant when the destabilizing RC terms are large relative to conventional production, characterized by S^2.

E. LES Sub-Grid-Scale Modeling

A sub-grid-scale (SGS) model is needed for LES simulations described in the next section. The SGS eddy-viscosity is provided by two of the DES models available in Overflow, with a modification. For this work which is focused on free shear flows, the terms LES and DES are effectively similar. The SA-DES turbulence model was used in the mixing layers which have no walls present, while the SST-DES model was used for the rocket plumes, in which the jet flows out of a small body (a 'pellet') with a short blunt nose and converging-diverging interior nozzle geometry. Both versions of the DES model have been altered. The conventional length scale $\mathcal{L}$ based on the grid spacing is scaled by an empirical function of the non-dimensional Q critereon

$$\begin{aligned} \mathcal{L} \;&\rightarrow\; \mathcal{L}\, F_Q(Q_{ND}) \\ Q_{ND} &= (R_{ij}^2 - S_{ij}^2) \,/\, U_{ij}^2 \\ F_Q &= 1 - [2.3]Q_{ND}, \qquad \text{limited by} \\ &= 1 \quad \text{for} \quad Q_{ND} < -0.2 \\ &= \max(F_Q, [0.3]) \end{aligned} \tag{15}$$

Vortex cores have $Q_{ND} > 0$, and in an ideal 2D vortex, $Q_{ND} = 1$ at the core. The primary effect of this change is to reduce the sub-grid-scale eddy-viscosity near vortex cores, which are *kRC* stabilized. This form of *kRC* modeling is Galilean-invariant. The model's behavior is linear near $Q_{ND} = 0$, so there is an increase in the length scale for $Q_{ND} < 0$. The net effect in shear layers has been to accelerate the development of fully turbulent flow, and give a more rapid approach to a fully-asymptotic state. This modeling did not notably reduce integration stability, but it is likely that the WENO convection algorithm and flux limiter were responsible for more of the dissipation than when the standard DES SGS model was used.

III. LES of Mixing Layers & Rocket Exhaust Jets

This study has relied on large eddy simulations of mixing layers and rocket exhaust plumes to create the data for use in tuning and preliminary validation of the TMRC model. The mixing layers involve combinations of M_c, density (temperature) ratio, and *kRC* and *bRC* effects intended to elucidate the layers' dependence on these parameters and enable heirarchical tuning of model coefficients. Crossflow, which involves a change of the direction of the mean vorticity vector across the layer, was included in a few simulation and found to cause a small (~10%) increase in layer growth rate. Simulations of several rocket-exhaust single plumes were done with a primary objective of characterizing the differences between cold and hot jets, at representative flight conditions for the Orion Launch Abort Vehicle (LAV). All simulations were done with ideal air as the gas.

The simulations were run using the CFD solver Overflow, and many details of the simulations are similar for the mixing layers and exhaust jets. The 5^{th}-order WENO spatial discretization scheme was used for the primary mixing-layer and plume regions in the CFD domain. For the jet, the 3^{rd}-order scheme with the flux Koren limiter was used in small region at the expected location of the Mach disk. The simulations were run on relatively fine grids, with small time steps. The hot and cold jet cases are run on grids with 360M grid points, while mixing layer grid sizes were variable and in the range of 45-212M points. Time advance was by Overflow's second-order sub-iteration scheme, that typically achieved 1.5 to 2 orders of magnitude inner-iteration convergence. The DES SGS eddy-viscosity was described above. Downstream of the regions of interest, the grid was gently stretched to a large streamwise grid spacing to suppress turbulence before it reached the outflow boundary. Most of the outflow boundary was treated with a characteristic outflow boundary condition, but the theoretical pressure was applied over small areas outside the turbulent regions. Inflow boundaries that lead to shear layers and at the rocket nozzle plenum were seeded with weak perturbations that were derived from random-number fields, that were smoothed and periodic in space and time; random temporal phase shifts were included. The mixing layer (ML) simulations were run with spanwise periodicity and slip walls at the minimum and maximum radii of the CFD domain. One challenging issue involved waves emanating from the ML at the inflow plane and reflecting at the top and bottom walls to then impinge on the mixing layer. To the extent possible, the domain was sized to give a long streamwise region of the ML that was free of reflected waves. Another challenge was avoiding reflected waves that could trigger the formation of large, mostly spanwise structures. Many low-speed ML simulations developed this behavior, typically if the domain was too small, or the grid stretching was insufficient. These results were discarded. For high-speed flows, sonic and faster inflow was often used to avoid this problem. The jet simulations were run in a large domain with a characteristic farfield.

A. MRC Mixing Layers

This section describes LES results for MLs affected by variable M_c and RC effects. It also includes TMRC results that have been tuned on the LES data; the agreement between TMRC and LES results is a product of this tuning and the "tunability" of the model. Results from the standard SST model, with and without conventional CC, RC and QCR modeling, are included. Planar mixing layers are an important subset of this work.

A ML is defined by its two freestream flows, each with constant stagnation pressure coefficient C_{p0} and entropy S, with a smoothed jump at the centerline of the ML. Curved flows have a centerline radius of curvature, R. In curved MLs, the 'freestream' properties like pressure and velocity vary in the radial direction, and the conditions at the edge of the ML evolve as the layer grows into this non-uniform freestream. This evolution affects many aspects of these flows, and their effects are addressed in the post-processing. When a specific flow is described, those ratios are determined when the layer is very thin. The flows can evolve to have weaker or stronger RC and M_c effects in the downstream direction, so achieving truly asymptotic behavior is difficult.

RC effects in low speed mixing layers depend on the mean-flow parameters: (1) streamline curvature quantified by δ/R, the ratio of layer thickness to radius of curvature, (2) the velocity ratio U_1/U_2, in which U_1 and U_2 are the two freestream velocities, and (3) density ratio ρ_1/ρ_2 across the mixing layer. The convention herein is for the velocity ratio to be larger than one, and the sign of curvature is used to distinguish between stable and unstable condition, with $\delta/R < 0$ denoting stabilizing conditions. This approach is not valid when working with combined *bRC* and *kRC* effects of opposite sign, but those conditions are not being presented here.

Mixing layer growth rates are typically normalized by $0.5(U_1 + U_2)/(U_1 - U_2)$ to make them Galilean invariant. In simple shear layers, $(U_1 - U_2)$ provides the shear which drives turbulence production. The average streamwise velocity $(U_1 + U_2)/2$ affects mixing layer growth in two ways. (1) It affects the convective term $u\partial*/\partial x$ in the Galilean invariant growth rate, which the normalization addresses, and (2) the mean velocity affects the radial pressure gradient in a curved mixing layer, and hence RC effects via the difference between convection which is $O(u)$ and the $O(u^2)$

pressure gradient. Thus, a ML has stronger relative RC effects at lower U_1/U_2, when other parameters are held constant. The growth rates $d\delta/dx$ of mixing layers are normalized this way, except for baroclinic-only mixing layer, in which $(U_1 - U_2) \sim 0$; those results are presented without normalization. The averaging of LES solutions is done over time and the spanwise (periodic) direction. The ML edges were taken to occur where the circulation had changed by 2%, relative to the full layer's change in circulation. See Matsuno[17] for the use of circulation in detecting the layers' edges in a curved-flow environment. The 2% edge criterion was applied to entropy in the baroclinic-only layer, in Figure 2.

1. Mixing Layer Examples

Two mixing layers are presented to illustrate the nature of the LES simulations. The first is the 'baroclinic-only' ML, which has essentially no shear across the centerline of the ML, but has an unstable 9-to-1 density ratio. It is an irrotational vortex flow, with $V \sim 1/R$; C_{p0} and S are constant on both sides of the ML centerline at a radius of 500. The release of potential energy causes turbulence to grow and the ML to spread rapidly. A shapshot of the vortical structure is given in Fig. 2. The initial conditions and the averaged flow field at three downstream locations extracted from the time-asymptotic state are given in Figure 3. This flow was run with $U = 1.5$ on both sides of the ML, with an average acoustic speed $a = 1$ at the centerline. At this high speed, there is a strong radial pressure-drop approaching the vortex core. To avoid $p \to 0$ at small radius, the velocity is reduced as shown in the figure. This velocity gradient is highly RC-stabilized and outside the turbulent region, so it does not generate turbulence and should be less-reflective of acoustic waves than a solid wall. This procedure was used in many ML calculations that involved high density and Mach number in the inner layer. The asymptotic state illustrate how the density and other variable are non-constant at the edge the ML. The initial density ratio of 9-to-1 falls to about 5-to-1 at the furthest-downstream profile in asymptotic state.

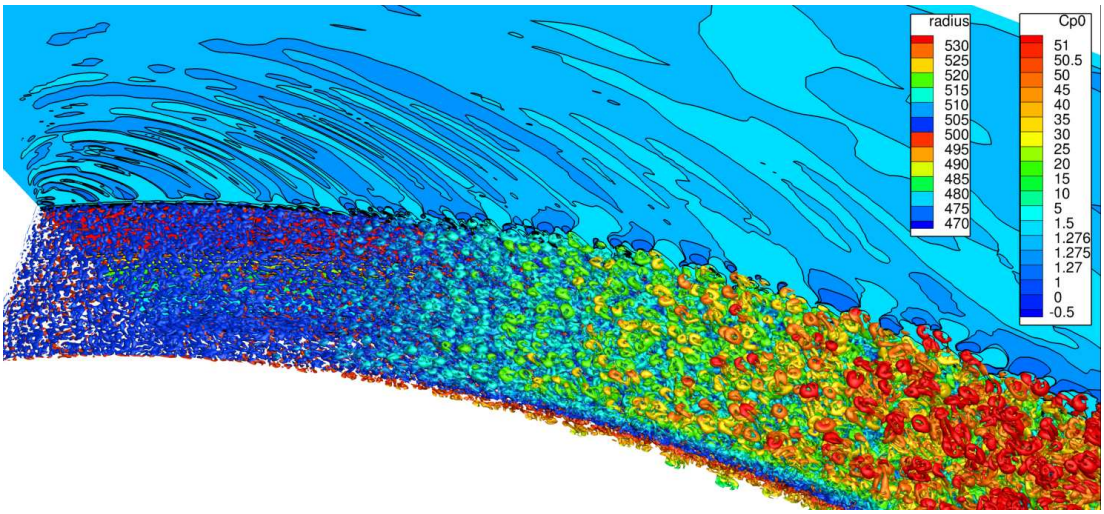

Fig. 2 Image of vortical structures on the high-pressure side of the baroclinic-only ML with $R_{CL} = 500$ and $\rho_1/\rho_2 = 9$. The isosurface is of $Q_{ND} = 0.005$, which is colored by the radius of that point on the isosurface. This visualization scheme is biased to highlight ring vortices surrounding 'puffs' of flow moving away from the centerline of the mixing layer. The 'back-plane' gives contours of C_{p0} which reveal acoustic waves originating at the inflow plane and hydrostatic fluctuations that travel with vortical structures. The non-linear C_{p0} contour levels were selected to emphasize these features. (In the full-resolution graphic, the dominant vortex-ring structures appear at the dark-blue/mid-blue boundary, at $radius = 505$.)

Figure 4 gives the layer thickness and layer growth rate for LES, the TMRC model and the stock SST model. All of the mixing-layer LES results exhibit a common pattern, involving three notable stages of development. (1) The initial LES mixing layer is poorly resolved and the inflow is seeded with smoothed random fluctuations confined to the mixing layer. This phase involves a latency period where the most unstable modes gradually dominate. (2) Next, the dominant modes exhibit exponential-like growth of 'low-Reynolds-number' turbulence. The thickness δ of the layer and its growth rate increase rapidly in the downstream direction. In the thin initial layer, the grid resolution only supports eddies that are large relative to the layer's thickness. Initially, there is insufficient resolution to capture the small scales that would 'nibble away' at the larger structures, but this deficiency is corrected with layer growth. The maximum

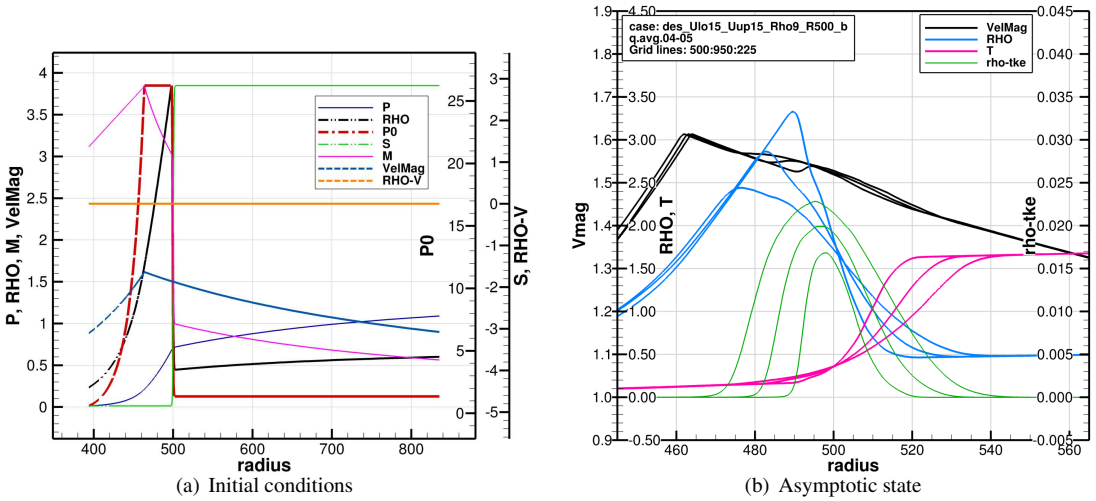

(a) Initial conditions (b) Asymptotic state

Fig. 3 Radial profiles of the (a) initial/inflow conditions, and (b) the averaged asymptotic state at three streamwise stations. Overflow's non-dimensional variables include static density (RHO), temperature (T) and pressure (P), isentropic stagnation pressure (P0), Mach number (M), radial momentum (RHO-V) and entropy(S). Initial profile has the primary mixing layer formed by smoothed step-profiles in P0 and S. In the asymptotic state, the profiles increase in width with increasing downstream distance.

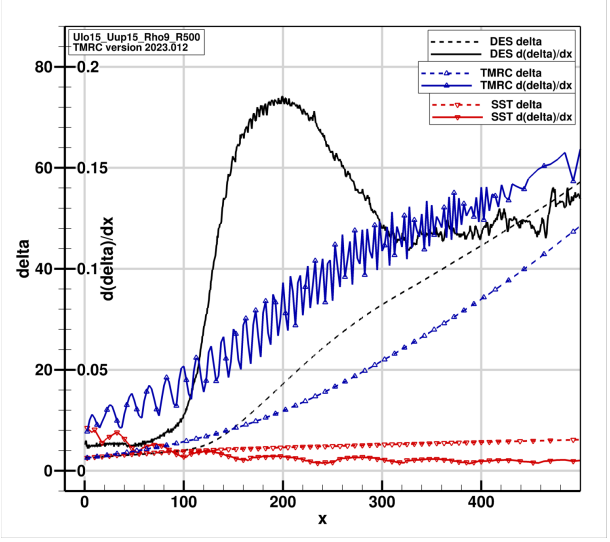

Fig. 4 Layer thickness δ and its growth rate $d\delta/dx$ for mixing layer driven primarily by the baroclinic instability, with results from LES, and RANS TMRC and the standard SST. (The jagged growth rates are due to noisy calculation of the layer's thickness.)

growth rate is achieved during this period. (3) Finally, the mixing layer approaches its asymptotic state before exiting the fine-grid region and flowing into the coarse-grid damping region of these spatially-developing simulations. The final decay to the asymptotic state can be very slow, and many simulations were affected by a too-short domain. The asymptotic state is used for model tuning.

Results from the TMRC model match the LES asymptotic growth rate reasonably well, but not the stages of latency and exponential growth. For cases affected by an RC instability, the asymptotic growth rate depends on δ/R, and as δ increases in the downstream direction, so does the asymptotic growth rate. The TMRC simulation clearly gives an increasing growth rate of with downstream distance. This trend appears to be present at $x \sim 300^{+}$ in the LES simulation,

but that is a bit ambiguous, due to the short region of flow that appears to be asymptotic. The TMRC coefficients were tuned to achieve good agreement of the streamwise evolution of the velocity profiles, but the layer's thickness and growth rate depend on the velocity profiles. There is no expectation that the stock SST model can perform well in this test as it lacks any sensitivity to the *bRC* mechanism, and it gives a growth rate close to zero.

The second flow to be considered in some detail is for $M_c = 0.1$, *kRC*-unstable with $U_1/U_2 = 2$ and with neutral *bRC* conditions. This flow is expected to develop an initial structure of spanwise Kelvin-Helmholz vortices that grow in size and streamwise spacing, with braid vortices. Several of these features are visible in the initial layer, but they are soon replaced by tangled 3D vortices. The contours of C_{p0} on the back-plane of the image shows a few acoustic waves propagating away from the ML inflow region; the hydrostatic C_{p0} fluctuations that convect with the turbulent structures show the initial growth in streamwise wavelength. The spanwise vortical structures and their hydrostatic Cpo signature are absent in the (streamwise) middle of the domain. The visual field of the Q_{ND} isosurface is dominated by two features. (1) 'Threads' of vorticity are the only structural feature seen in the Q_{ND} isosurface. Many of these are in the geometric form of loops whose tops tend to be tilted, on average, toward the inflow. The upper freestream is slow, so the tilt can be thought of as the result of drag by the slow upper freestream exerted on structures in the ML moving at roughly the mean centerplane velocity. The lower surface exhibits similar vortices, but tilted in the downstream direction by that freestream's higher velocity. Also, the vorticies tend to align with the principal elongational axis of the strain tensor. (2) There are two distinct spanwise regions of streamwise oriented ridges of turbulence, in the downstream half of the visible ML, which are suggestive of a pair of Görtler-like structures. Q_{ND} is non-dimensional, and does not explicitly favor small scale vortices over large ones. Observe in Fig. 2 that the small ring vortices in the early layer are visually similar to larger versions in the downstream layer; their change in scale does not alter the visualization linked to a specific value of Q_{ND}. Large scales are easier to distinguish from the turbulent noise of small scales by using the radial displacement, which conceptually results from a double integration of the vorticity, firstly to obtain velocity, and secondly to obtain displacement. There is also a hint of a spanwise structure, accompanied by a signal in C_{p0} on the backplane of the image, in this downstream region. Significant differences can be seen in the small-scale vortical structures of the baroclinic-only layer in Fig. 2 and this shear-dominated layer in Fig. 5.

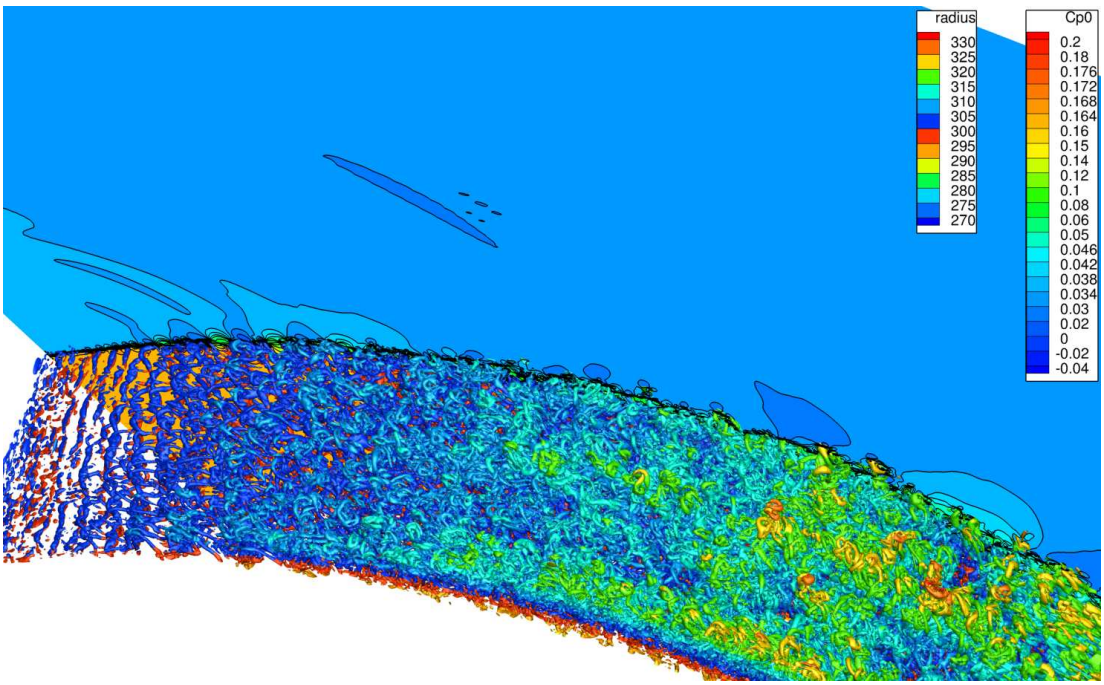

Fig. 5 Image of ML vortex structures, visualized as in Fig. 2, viewed from the high-pressure side of the ML that is *kRC*-unstable with $U_1/U_2 = 2$, with neutral *bRC* conditions, and at $M_c = 0.1$. Streamwise-aligned ridges exist in the downstream layer suggest the possibility of Görtler-like structures.

2. Planar Layer M_c Effects

The growth rate of a planar mixing layer as a function of M_c is one of the primary model-tuning targets. Results from LES and TMRC are given in Fig. 6. Recall that the layer edges are defined as being 2% in from the edge value of the circulation (here, velocity), for LES and RANS, which will report a thinner layer and lower growth rate than a 1% edge condition used by some researchers. First, consider the LES results. The growth rate at $M_c = 0.1$ is $d\delta/dx = 0.095 \pm 0.02$. The largest uncertainty in the present LES results occurs at $M_c = 0.1$. Two results from the present work are given at this M_c. Both appear to be of high quality with no obvious defects, but they differ in growth rate by $\sim\pm 10\%$ about their mean value. The low-speed growth rate is a source of uncertainty in experimental measurements of this flow. Slessor[16] notes there is a substantial variance of $\sim\pm 30\%$ in ML growth rate. Acoustic feedback and insufficient domain length are the primary suspected causes of this variability. All low-speed LES cases that exhibited acoustically-forced HK waves were excluded from this study, but that detection process had limited precision. With increasing M_c, the growth rate initially falls sharply and is then roughly constant to within the uncertainty estimates for $M_c \geq 2$. This general trend is consistent with Rossman's[18, 19] measurements and aggregation of other data at high M_c. However, the total reduction in growth rate between $M_c \sim 0$ and 4 in these results is less than in most other results. It is not possible to attribute this difference to the rates at low or high M_c, because most studies report data normalized on the low-speed growth rate. Simulations by Matsuno[17] also give a smaller reduction in growth rate than is commonly reported in the literature.

The TMRC model gives growth rates that fall within the uncertainty estimates for the LES results. However, the modeled trend does not become as close to constant at elevated M_c as seen in the LES results and experimental literature.

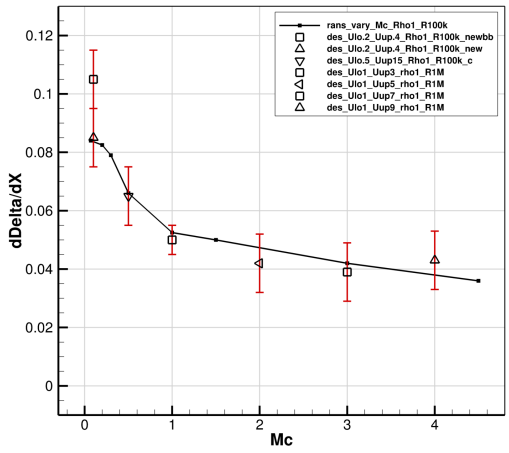

Fig. 6 Growth rate versus M_c for planar mixing layer with unity density ratio, for TMRC RANS and DES. Error bars on LES results are human estimates.

3. M-RC Interactions

The next set of flows presented here involve curved mixing layers at elevated M_c, and the objective is to quantify the interaction of RC and CC effects. The 'barrel' sections of rocket plume shear layers involve a combination of *kRC* instability and the suppression of mixing due to elevated M_c. Hot plumes experience *bRC* stability, while ambient-temperature plumes are *bRC* neutral. In the compressions between the barrel sections, streamline curvature and these stability characteristics are reversed. The work presented here considers only *bRC* neutral conditions. An important assumption in prior work with the SST-MRC model[6] was that unstable RC effects dominate the CC effect, so RC-unstable layers grow rapidly even if M_c is elevated. The goal of the LES calculations is to quantify how these competing influences interact.

Figure 7 gives the growth rates of mixing layers for range of $0.1 \leq M_c \leq 2.0$ and RC effects in the range of $-0.1 < \delta/R \leq 0.15$, computed with LES and RANS models. Both LES and RANS are computed on domains similar to those in Fig. 5, with a nominal fixed central radius of curvature; however, the RANS cases are 2D and have a coarser streamwise grid spacing. The M_c and U_1/U_2 used to name the cases are taken from the initial conditions. The change in layer thickness δ and its dependence on the actual edge velocities is included in the post-processing. All trend data are

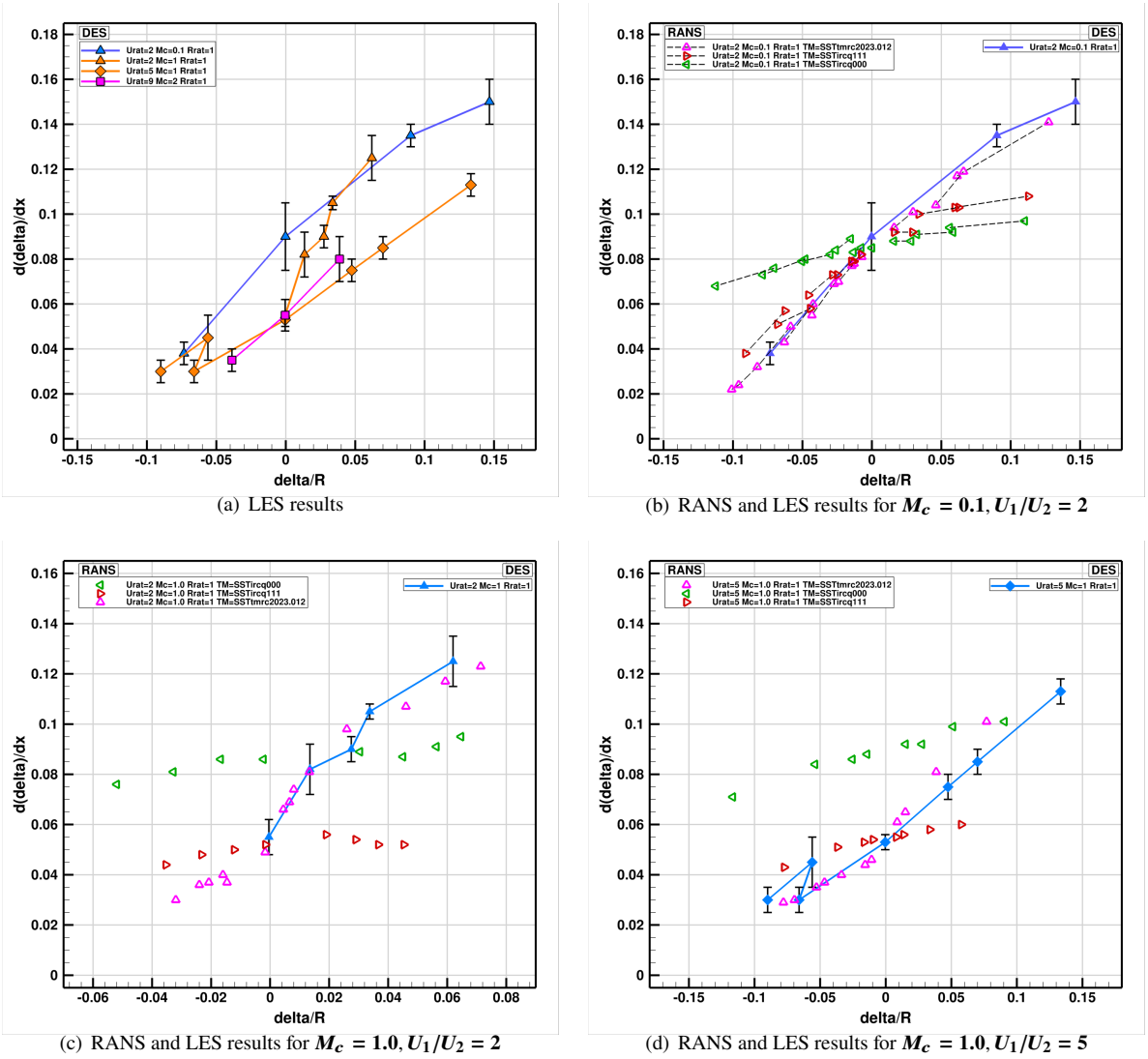

(a) LES results

(b) RANS and LES results for $\boldsymbol{M_c = 0.1, U_1/U_2 = 2}$

(c) RANS and LES results for $\boldsymbol{M_c = 1.0, U_1/U_2 = 2}$

(d) RANS and LES results for $\boldsymbol{M_c = 1.0, U_1/U_2 = 5}$

Fig. 7 The growth rate of mixing layers with variable M_c and RC effects, and a unity density ratio. Stable RC conditions are indicated by $\delta/R < 0$. Error bars are subjective judgments of the uncertainty in the asymptotic growth rate. Urat and Rrat in the legend are velocity and density ratios across the initial layer. (Note the different x-axis range in plot (c).)

composites of multiple CFD runs, for LES and RANS, needed to span a wide range of δ/R. The set of simulations used in this section differs from the simulations used in the previous section. Some results appear to be slightly out-of-family, presumably due them being less than fully streamwise-asymptotic, and they serve as an approximate measure of the uncertainty in the process of computing $d\delta/dx$.

Figure 7(a) includes only LES results. The growth rate at $M_c = 0.1$ and $U_1/U_2 = 2$ is $d\delta/dx = 0.09$ for a planar layer ($\delta/R = 0$), which falls to $d\delta/dx \sim 0.04$ at $\delta/R \simeq -0.07$ and rises to $d\delta/dx \simeq 0.15$ at $\delta/R \simeq 0.15$. At $M_c = 1.0$ and $U_1/U_2 = 2$, the planar layer grows at $d\delta/dx \simeq 0.045$ which is $\sim$50% of the low-speed growth rate. The growth rate increases with δ/R and by $\delta/R \sim 0.03$, the growth rate of this $M_c = 1.0$ layer matches that of the layer at $M_c = 0.1$. This results confirms the speculation that destabilizing RC effects over-power stabilizing CC effects. For $M_c = 1.0$ and $U_1/U_2 = 5$, destabilizing RC effects also over-power CC effects, but do so more slowly with increasing δ/R. LES results for $M_c = 2.0$ and $U_1/U_2 = 9$ are included, but they do not differ from results at $M_c = 1.0$ and $U_1/U_2 = 5$ when

uncertainty estimates are considered. The two results with $M_c = 1$ demonstrate a dependence on the velocity ratio, which is attributed to mechanisms discussed near the start of Section III.A.

RANS results are included in Fig. 7(b-d) for the following turbulence models: TRMC; stock SST with no modifiers; and SST with with the combined effects of three common modifiers, the SST-adapted RC part of the SARC model, the CC model of Suzen and Hoffmann and QCR2020. The notation 'SST-*ircq000*' indicates that (RC, CC, QCR) modifiers are (off,off,off). The TMRC model has its own version of these three modifiers enabled simultaneously, making the 'SST-*ircq111*' (on,on,on) model option the most similar to TMRC. (This naming scheme is derived from Overflow's model option settings.)

Figure 7(b) gives results at $M_c = 0.1$, and $U_1/U_2 = 2$. The stock SST model gives about 30% of the reduction in $d\delta/dx$ relative to LES for stabilizing condition and 20% of the increase for unstable conditions. This RC sensitivity results naturally from the difference in S and ω (true vorticity) in curved flows, and is an important component of the physical RC mechanism: reduced strain closer as the flow becomes more like a vortex core. The SST-*ircq111* option gives about 80% of the reduction in $d\delta/dx$ seen in the LES. The increase in $d\delta/dx$ for unstable conditions agrees reasonably well with LES for $\delta/R \leq 0.03$, but for larger δ/R, the results parallel the SST-*ircq000* behavior. This trend results from the limiting to achieve $Fr1 \leq 1.25$ in the RC modeling from the SARC model, at which point, the natural dependence on S and ω in curved flows determines the behavior for larger δ/R. The TMRC model is generally within 0.005 of matching the $d\delta/dx$ from LES over the entire range of results presented.

Figure 7(c) gives results at $M_c = 1.0$ and a velocity ratio of 2, for which LES was only run at RC neutral and destabilizing conditions. Elevated freestream Mach numbers, here 2 and 4, lead to shocklets at the layer's edge and an increase in the uncertainty in measuring $d\delta/dx$. The stock SST model, SST-*ircq000*, results are similar to its behavior at $M_c = 0.1$ and are not close to the LES data. The SST-*ircq111* set of model options gives $d\delta/dx$ results that roughly parallel the stock SST results, but reduced by about 0.035. The SST-*ircq111* result agrees with LES for $\delta/R = 0$, but predicts essentially no increase in $d\delta/dx$ with increasing δ/R; it predicts only $\sim 50\%$ of the LES growth rate by $\delta/R \sim 0.04$, and exhibits no tendency to improve at higher δ/R. The TMRC results are in good agreement with LES, with differences in $d\delta/dx$ less than 0.01 over the range of the LES data. Note that the TMRC and SST-*ircq111* results differ $\delta/R < 0$. Both models have RC and CC modeling active, those effects should be 'additive' in some sense, but their net effects differ substantially. Unfortunately no LES results are available for this set of ML parameters.

Figure 7(d) gives results at $M_c = 1.0$ and a density ratio 1, but now with a $U_1/U_2 = 5$. As discussed above, the higher velocity ratio reduces the mean velocity and which reduces the strength of *kRC* effects. Thus, the influence of *kRC* on the CC effects is expected to occur at larger values of δ/R, relative to the behavior at $U_1/U_2 = 2$. The LES results display this trend clearly in Fig. 7(a), as do the TRMC results in Fig. 7(d). The TMRC model tends to slightly overpredict the LES growth rate for *kRC*-unstable conditions. TMRC results are close to the LES data for *kRC*-stable conditions, but the LES data exhibit relatively large uncertainty among runs at similar δ/R. As in Fig. 7(c), there is no modeled M-RC interaction for RC-stable conditions; this suggests that the TMRC results could be reasonably accurate at those conditions.

B. Single LAV Exhaust Jets

The next flows to be considered involve a single jet in a free-stream that mimics the configuration and operating conditions of single Abort Motor (AM) plume on the Orion Launch Abort Vehicle (LAV). The jet emerges from a small body called a 'pellet' that is just large enough to enclose the rocket nozzle's interior, with a rounded nose. The rocket nozzle exhausts into a freestream at 25° incidence angle, to match LAV AM plumes that are canted 25° outward. The scale-resolving simulations of the pellet problem are DES, as there is attached RANS boundary layer flow on the pellet body, and these simulations are run with the SST-version of DES, including the scaling of length scale as in Eqn. 15. The inflow to the plenum of the jets was seeded with weak unsteady perturbations. Figure 8 shows only half of the CFD calculation (for clarity) including pellet body with Cp contours and the instantaneous turbulent structure in the exhaust jet. The stagnation point can be seen on the lower part of the pellet's nose, and a separated wake is visible above the pellet body. Results from two simulations are presented, both at the same vehicle-based thrust coefficient of $CT = 3$ and a freestream Mach number $M_\infty = 1.3$, but with differing jet plenum temperatures of $500R$ (cold) and $5000R$ (hot).

Gross characteristics of the jets are expected to influence turbulence in predictable ways. Hot and cold plumes have similar patterns of Mach number on the symmetry plane as shown in Fig. 10 and Fig. 12. Thus, the 10× hotter plume has roughly 3.3× higher velocity and with 10× lower density. Density and velocity differences alter the magnitude of the three primary turbulence-generation mechanisms: the stress-strain S^2 term, and the baroclinic and kinematic RC terms. In the primary barrel shear layer of the hot plume, the *bRC* mechanism should reduce turbulence, while the S^2

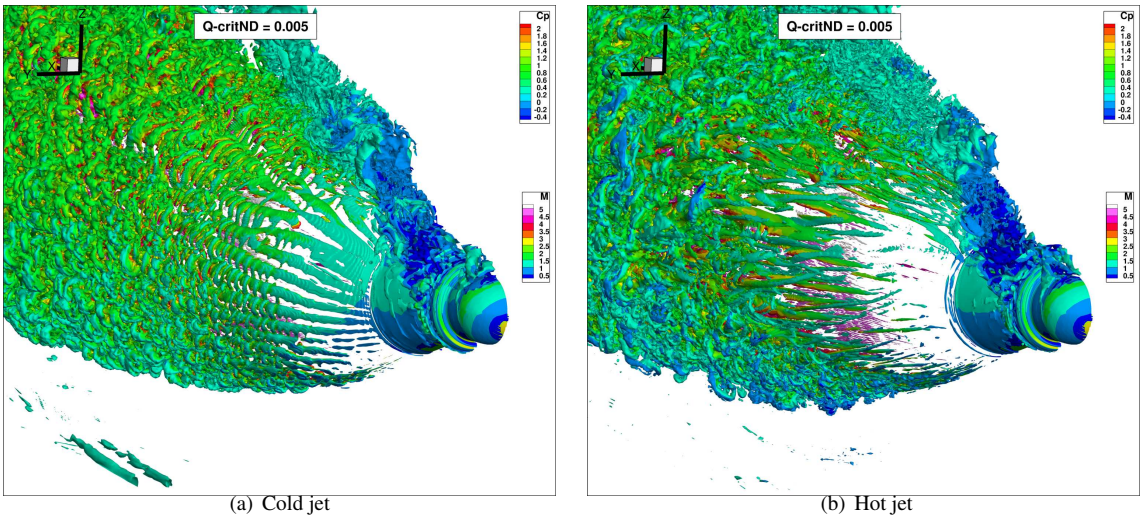

(a) Cold jet (b) Hot jet

Fig. 8 Isosurface of Q_{ND} = 0.005 colored by Mach number contours, and Cp color contours on the pellet body, for an instantaneous DES flow field. Only the half-domain nearest the viewer is plotted, to more clearly show turbulent structures.

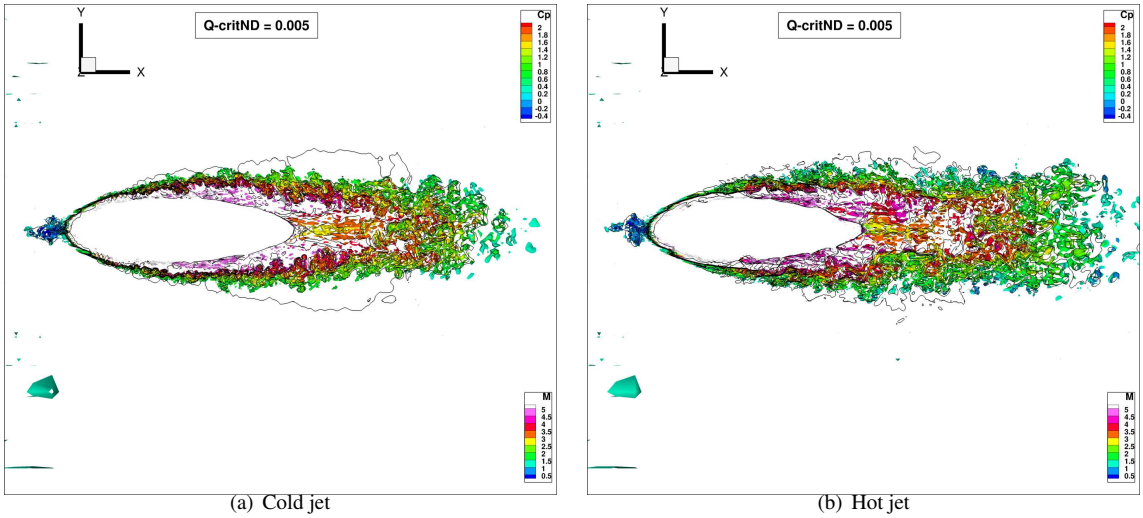

(a) Cold jet (b) Hot jet

Fig. 9 Isosurface of Q_{ND} = 0.005 colored by Mach number contours and black line contours of Cp, in a thin volume above the nozzle body, for an instantaneous LES flow field. The hot-jet (b), relative to the cold one(a), exhibits a more perturbed barrel shock with more turbulent structures downstream of that shock, thicker shear layers and a wider downstream jet.

production should increase it. In the cold plume, the absolute maximum velocity is limited to $\sim 2.5a_\infty$ by basic gas dynamics, which, with $M_\infty = 1.3$, further limits the maximum velocity difference and strain rate available for turbulence generation in the plume shear layer. The net effect appears to be a higher level of turbulence in the hot jet. These single jets combine many of the mean-flow phenomena relevant to turbulence in LAV and SRP plumes, including a wide range of RC effects, high Mach number, crossflow and the jet's subsequent roll-up into a vortex pair, and the effects of transverse curvature in addition to streamwise curvature. The majority of turbulence physics know to occur in LAV plumes is amenable to steady RANS modeling.

Figure 8 gives an image of the instantaneous structure of the resolved scales visualized by an isosurface of the non-dimensional Q criterion $Q_{ND} = 0.005$, which is colored by the local Mach number. In a complex flow such as this plume $Q_{ND} \sim 0.2$ appears to highlight strong vortex cores, while $Q_{ND} = 0.005$ identifies more general vortex

structures, and hence regions of turbulence. Lacking a length scale, Q_{ND} is equally sensitive to large and small scales. These images appear to be dominated by small scales, while clumps of small scales make larger scales visible. Images from cold and hot plumes are given. They are generally similar in overall structure but differ in many details. The initial structures in the plume shear layer are quasi-streamwise-oriented crossflow vorticies, which are promoted in part by crossflow from the $\sim 25^\circ$ misalignment across the shear layer between the jet flow and the freestream. The streamwise vortices emerge more slowly in the hot-jet shear layer, but then large eddies develop more rapidly when the flow becomes "fully" turbulent. This initial region is the most likely to suffer from artifacts of it being a simulation, not a physical experiment. In the fully turbulent region, the visual structure of the shear layer is dominated by hairpin/loop vortices, whose outer extents are tilted upstream as in Fig. 5. For the selected Q_{ND} isosurface level, these structures in the hot plume mix more deeply into the freestream flow, as indicated by the lower Mach number contours on the outer eddies. The wake above the pellet body is fully turbulent. Figure 9 gives the same Q_{ND} isosurface looking down on a thin planar volume just above the upper lip of the nozzle. This slice of the flow is fully turbulent with many structures across the shear layer, with larger structures and intermittency at the layer's edge. Line pressure contours reveal the barrel shock, which is inside the shear layer. The plume deflects upward out of the visualization plane at the right side of the figure. Relative to the cold jet, the hot plume's shear layer appears thicker and has more wiggles in the barrel shock's shape, presumably caused by perturbations from larger turbulent eddies.

The next several figures demonstrate the agreement between the time-averaged DES results and RANS calculations with the same three modeling options used above, TMRC, stock SST-*ircq000* and SST-*ircq111*. The DES solutions are averaged over tens of thousands of time steps. The gross characteristics of the averaged solutions are well converged, but there also small-scale details that changed with each additional run added to the total averaged solution. Gradient quantities like vorticity are most sensitive to the state of asymptotic convergence of the average. The RANS solutions are also averaged over a short time interval. The stock SST solution tend to be steady; SST-*ircq111*, and the TMRC solutions can experience small fluctuations in the upper side of the jet. This is the leeward side with respect to the freestream, and the unsteadiness is roughly similar to Strouhal shedding that occurs in subsonic flow past bluff bodies. The plotting-scheme is similar in all of these figures. DES results are given with color contours, separated by white lines. RANS results are given as black contour lines with levels that match the DES contours, and dashed lines are used for negative levels. Good agreement is achieved when the black lines are coincident with, and obscure, the white ones.

1. Cold Jet RANS Comparisons

The cold-jet results, in Fig. 10 and 11 give contours of the Mach number on the $y = 0$ plane of symmetry and of x-vorticity at two x-stations, $175''$ and $245''$. The Mach number contours shows the shock cell shape, and shear layer thicknesses. The x-component (roughly streamwise) of vorticity is a critical element of the solution, as vorticity governs how the jet rolls-up into a pair of counter-rotating vortices and entrains fluid into the plume. Results are presented for the instantaneous TMRC solution and for averaged solutions given by all models. The instantaneous TMRC solution for the lower shear layer (as located in the figure) is about $\sim 10\%$ thinner than predicted by LES, while the upper shear layer is very different due to unsteadiness. Averaging smooths-out the ripples and causes the upper shear to agree very well with LES, while it has no visible effect on the lower shear layer. Measurable unsteadiness is confined to the leeward side of the jet. The barrel shock is in very good agreement in RANS and LES solutions. Its shape is dominated by inviscid phenomena, but the shear layer's thickness and growth rate cause meaningful variations in the shock shape. Both non-TMRC SST calculations underpredict the length of the shock cell by a very small fraction, whereas the averaged TRMC solution exactly matches LES, to plotting accuracy. The small spot of low Mach number in the upper-right part of the figures shows a related error: the shortened shock cell causes that feature to shift forward and match LES. In the results for modeling with SST-*ircq000* and SST-*ircq111*, both upper and lower barrel shear layers are too thin in comparison to LES. The first of these lacks an RC model, while the other has a CC model that is not sensitive to destabilizing RC effects.

The x-component of vorticity in Fig. 11 is generated by the crossflow due to the 25° angle of incidence. This flow has x-vorticity distributed around the jet with notable concentrations on the upper (leeward) side, which is the primary vortex pair. The vortex pair is present near the top of the plume in all of these figures. The TMRC and stock SST models give generally similar results in good agreement with the LES data; the most notable difference occurs in the small counter-rotating vortices arrayed in a $\times$ pattern near the core of the plume at $x = 245''$. The SST-*ircq111* model predicts the layer of x-vorticity to be much thinner than LES.

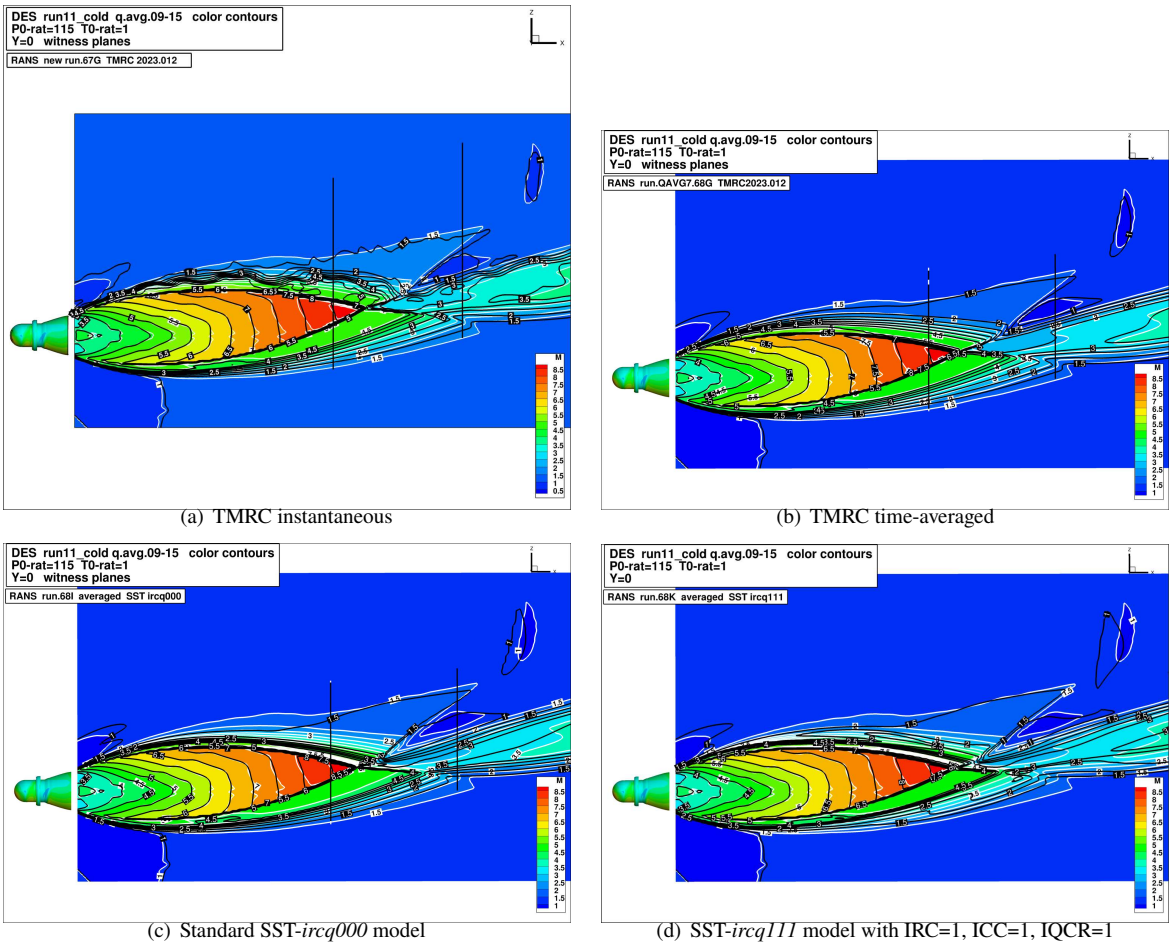

(a) TMRC instantaneous

(b) TMRC time-averaged

(c) Standard SST-*ircq000* model

(d) SST-*ircq111* model with IRC=1, ICC=1, IQCR=1

Fig. 10 Mach number contours on the vertical plane $y = 0$ (plane of symmetry), for the cold jet. Color contours are DES; Black lines are RANS TMRC. Vertical black lines are the $x = 175''$ and $x = 245''$ stations, where x-vorticity data are plotted.

2. Hot Jet RANS Comparisons

The results for the hot jet are given in Fig. 12 and 13 and include similar Mach number and x-vorticity plots. The first thing to note in the LES results is that the primary shock cell in the hot jet is shorter than in the cold jet. The plume shear layers are thicker in the hot jet, in which its higher sound speed, velocity and strain rate are expected to be a driving mechanism for elevated turbulence. The higher shear layer growth rate tends to 'push in' on the flow and shorten the shock cell. All RANS results predict the barrel shock to be a bit outside the LES shock, but the LES shock is also notably thicker than the RANS shocks, so the difference is less than it appears. The instantaneous shock shapes for the LES, in Fig. 9, exhibit larger waviness in the hot case than in the cold case, which is likely due to the more vigorous turbulent structures seen in the Q_{ND} plot for the hot jet, given in Fig. 8. For the hot jet, the SST-*ircq000* and TMRC models give roughly comparable accuracy for the plume shear layer thicknesses. As in the cold jet, the TMRC solution is unsteady in the upper shear layer, and the average TMRC gives better agreement with LES than does the SST-*ircq000* solution, which is steady. The SST-*ircq111* model again gives shear layers that are very much too thin.

The x-vorticity plots reveal more interesting patterns in the hot jet than in the cold jet. Because of the shorter shock cell and more rapid shear layer growth, there is only the tiny region inside the barrel shock that is free of x-vorticity at the $x = 175''$ station. The roll-up into a vortex pair is better developed, that is, more of the x-vorticity is concentrated in the vortex pair, while the same-sign x-vorticity around the core region has aggregated into several small 'messy' regions. The jet's shear layer is not distinctly identifiable in the x-vorticity contours, as it was in cold jet. In the cold jet, the x-vorticity is primarily of a single sign on each side of the centerplane. The hot case has the same primary vortex pair,

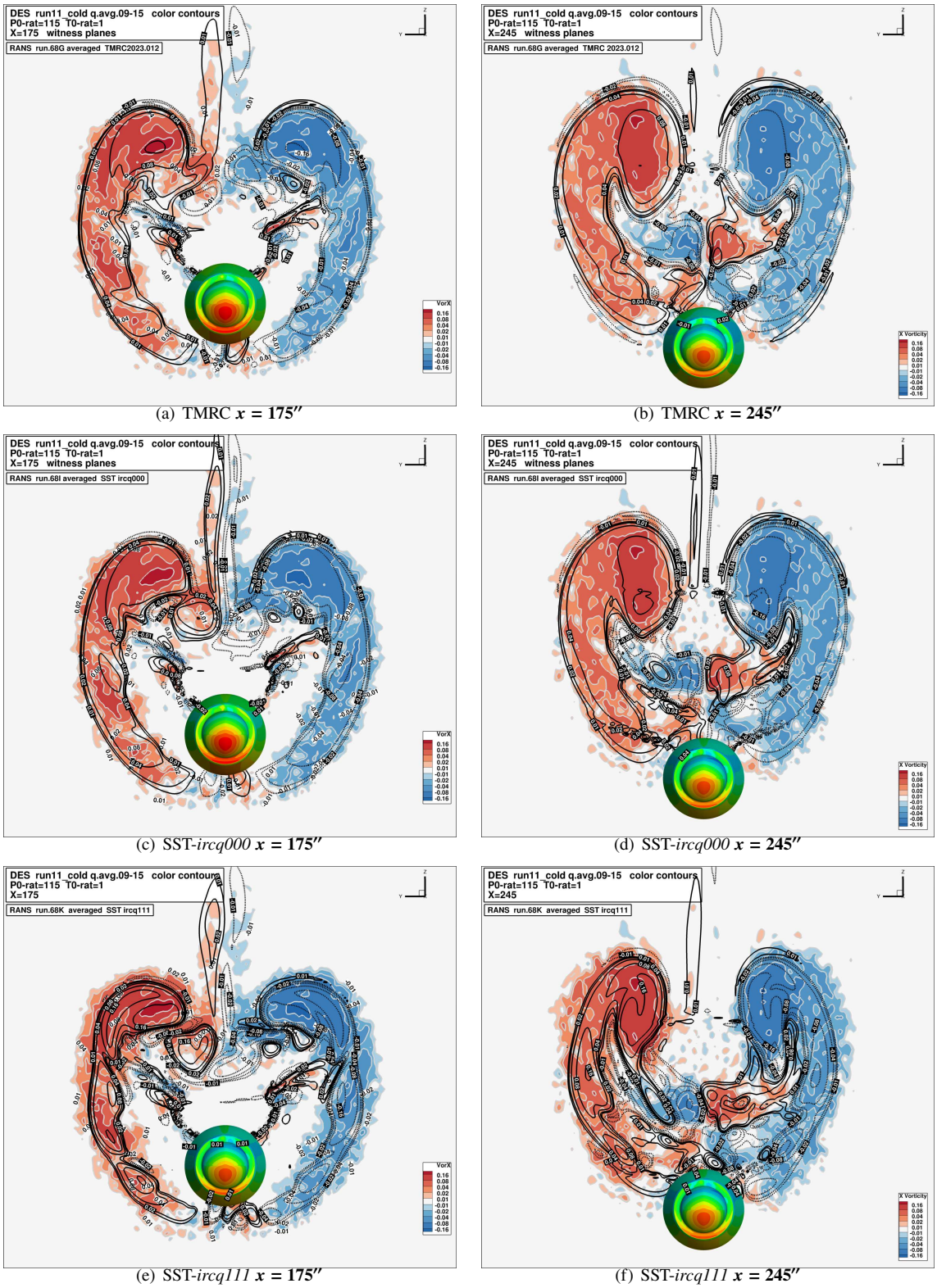

(a) TMRC $x = 175''$ (b) TMRC $x = 245''$

(c) SST-*ircq000* $x = 175''$ (d) SST-*ircq000* $x = 245''$

(e) SST-*ircq111* $x = 175''$ (f) SST-*ircq111* $x = 245''$

Fig. 11 X-vorticity contours for the time-averaged solution for the cold jet at two x-stations, $x = 175''$(left) $x = 245''$(right). Color contours are DES; Black lines are RANS.

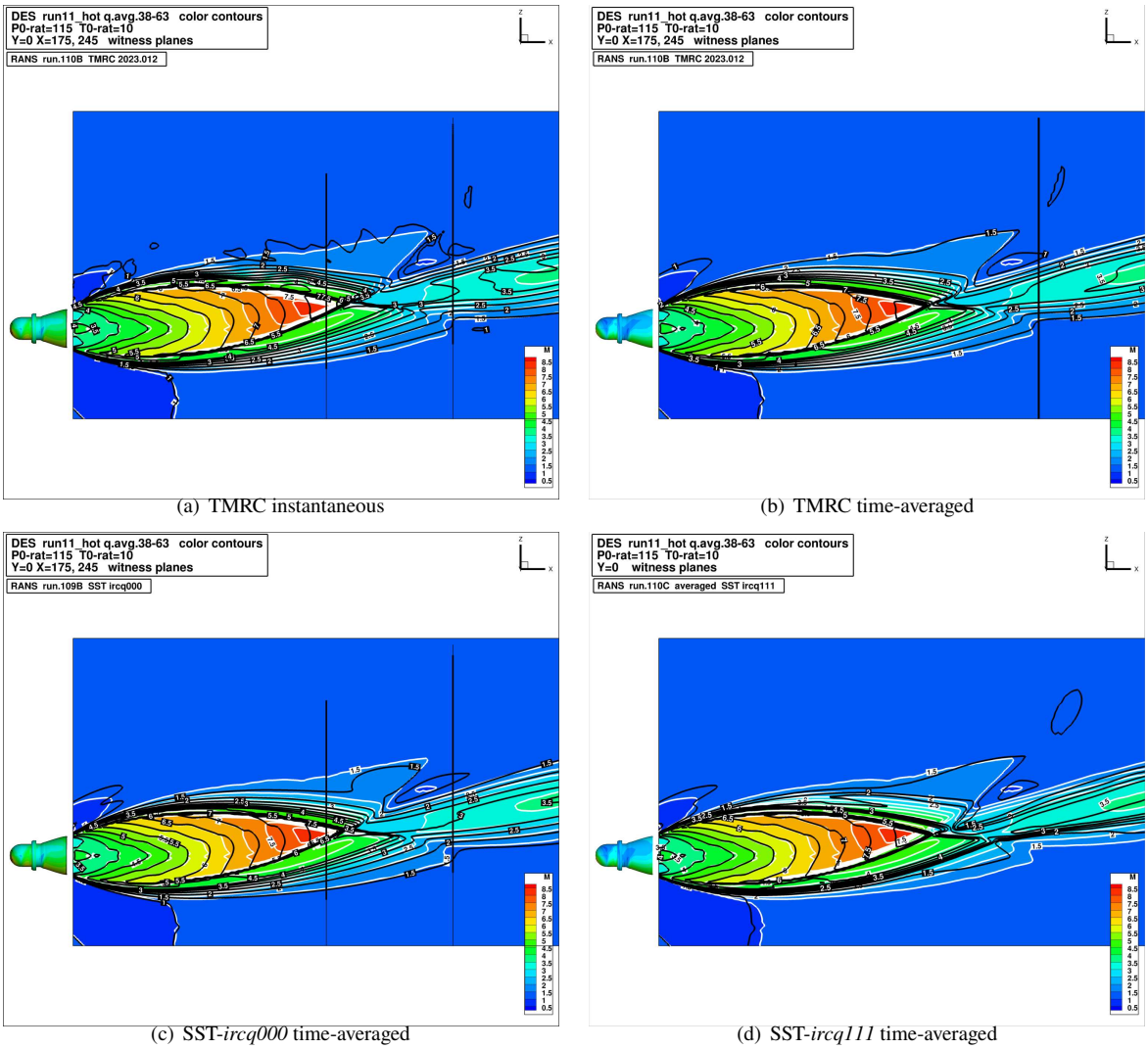

(a) TMRC instantaneous

(b) TMRC time-averaged

(c) SST-*ircq000* time-averaged

(d) SST-*ircq111* time-averaged

Fig. 12 Mach number contours on the vertical plane $y = 0$ (plane of symmetry) for the hot jet. Color contours are DES; Black lines are RANS TMRC.

but there is a substantial outer 'fringe region' in which the x-vorticity has the opposite sign of the primary vortex on that side. It is now worth noting that this fringe region exists in the cold jet RANS solutions, but it is very small.

The plots of x-vorticity show a greater difference between the TMRC and both SST models in the hot jet than was seen in the cold-jet. In the simplest sense, the TMRC model tends to slightly under-predict, while the SST-*ircq000* model over-predicts, the size of the plume's major features, and by implication the turbulent diffusivity. The SST-*ircq111* model gives a misshapen jet that is much smaller than the DES result. The TMRC model gives good accuracy for the shape and peak vorticity in the primary vortex pair at both x-stations, and the four vortices in an "×" pattern at the core of the jet at $x = 245''$. TMRC underpredicts the outer extent of the fringe-region. The stock SST model predicts the primary vortex pair to have too-low peak vorticity and a too-large radius, while the four vortices at the jet's core and the lower fringe region are reasonably well-predicted. In addition to the primary vortex pair, there is a tendency for the vorticity adjacent to the pellet (as it appears in the 2D image; in 3D, it is well downstream) to aggregate into clumps at $x = 175''$. All three modeling options exhibit this trend, with varying strength.

A primary objective of this model development work has been to gain understanding and improved modeling of the differences in hot and cold rocket exhaust jets. The TMRC model provides similar modeling accuracy for hot and cold jets - it tends to slightly underpredict the outer extent of the x-vorticity for both temperatures inFig. 13 and Fig. 11.

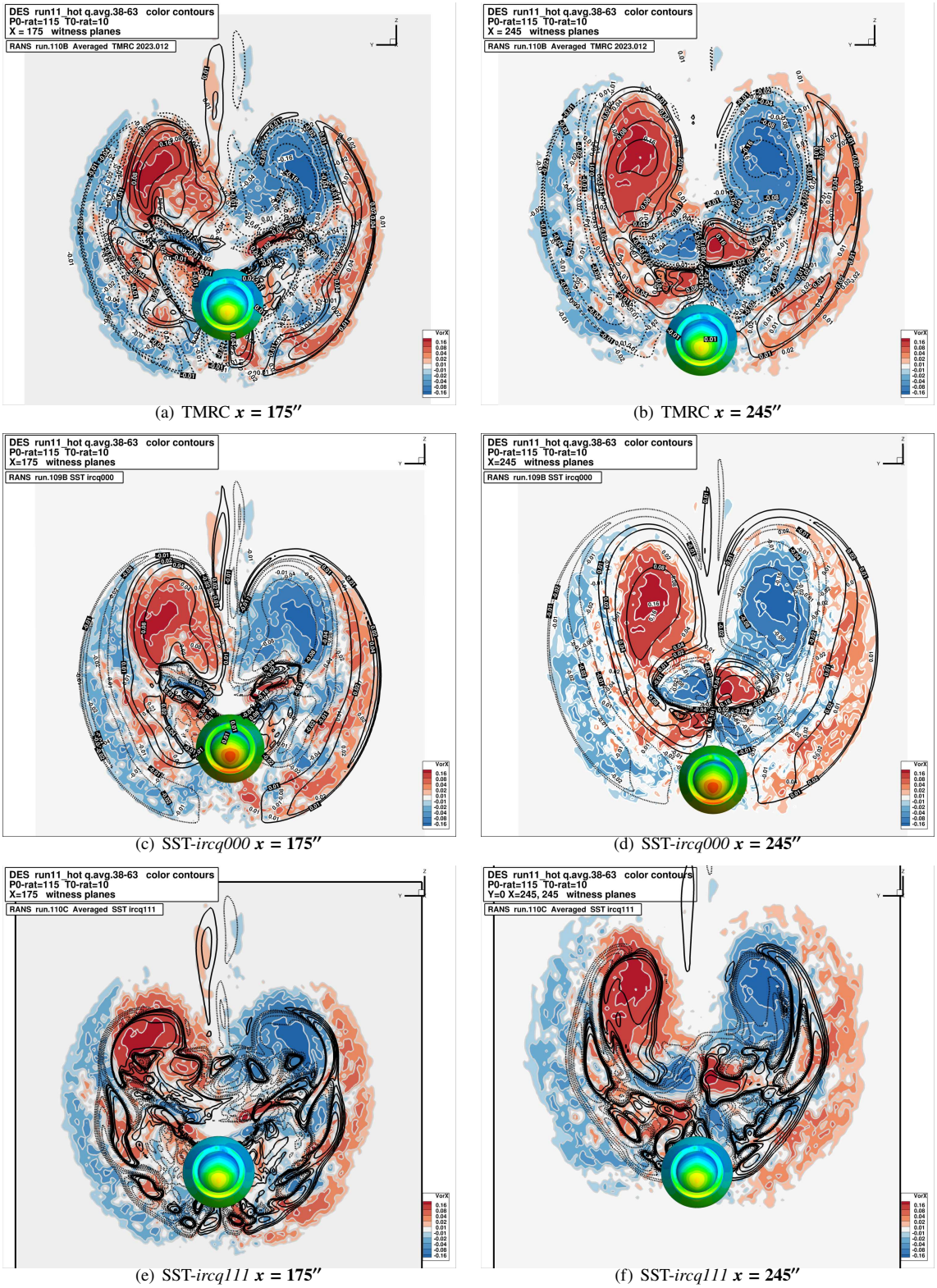

(a) TMRC $x = 175''$ (b) TMRC $x = 245''$

(c) SST-*ircq000* $x = 175''$ (d) SST-*ircq000* $x = 245''$

(e) SST-*ircq111* $x = 175''$ (f) SST-*ircq111* $x = 245''$

Fig. 13 X-vorticity contours for time-averaged solutions for the hot jet at two X-stations. Color contours are DES; Black lines are RANS.

The SST-*ircq000* model exhibits a notable difference in accuracy for hot and cold jets, giving accuracy comparable to TMRC in cold jets, but too much diffusion of x-vorticity in the hot jet.

IV. Supersonic Retropropulsion on CobraMRV

Supersonic retropropulsion (SRP) has been studied for decades, as it provides a means of landing large payloads on Mars despite its low-density atmosphere. A convergence of opportunities has led us to testing the TMRC model on SRP flows about a Mars entry, descent and landing (EDL) concept vehicle named CobraMRV which was recently tested in a physical experiment.[20–22] The companion paper by Matsuno [8] describes the CFD process and provides comparisons with experimental pressure and Schlieren data. Key features of the CFD methods applied to the regions of the plumes for these results are the following. The CFD solver is Overflow, which is being run with adaptive mesh refinement, third-order spatial discretization for RANS and fifth-order for DES, second-order time accuracy with roughly two orders of magnitude inner-iteration convergence, and the original SST DES model, but modified by the RC option given in Eqn. 15. The results presented in this section are based on the same set of CFD results as Matsuno, but delve into details of how differences in turbulence modeling lead to differences in vehicle aerodynamics.

The heatshield pressure is strongly affected by the shape of the bow shock around the stagnation streamline. Having areas of oblique shock leads to lower shock losses and higher surface pressure, while normal shocks lead to higher losses and lower pressure. The shape of the bow shock results from a complicated balance of the initially uniform inflow, altered by shock losses, which then reaches a quasi-stagnation surface, supported by back pressure from the SRP jets. Jets that remain compact and achieve greater forward penetrate provide less-uniform back pressure, which can cause more of the bow shock to be more oblique. The jets' spreading rate is governed by turbulence, so for this specific aspect of the SRP flow, there tends to be an inverse relationship between plume turbulence and heatshield pressure. It also means that improve RANS accuracy for rocket plumes may lead to improved accuracy for heatshield pressures during SRP. Matsuno [8] reports that the TMRC model is competitive with DES for predicting heatshield pressures at many operating conditions. This Section focuses on a flight condition for which all CFD results are in very poor agreement with experiment, and TMRC accuracy is inferior to that of DES.

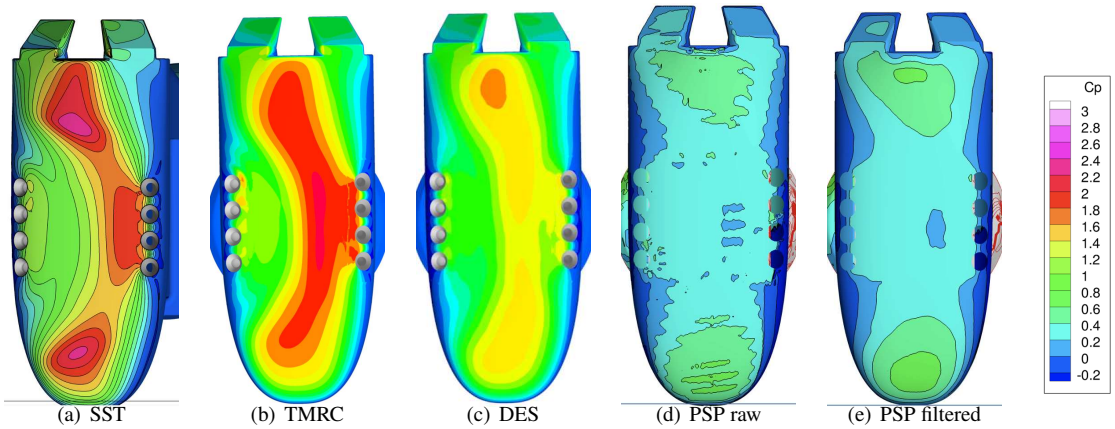

(a) SST (b) TMRC (c) DES (d) PSP raw (e) PSP filtered

Fig. 14 Heat shield C_p from averaged solutions for stock SST, TMRC and DES, and from raw and filtered PSP measurements.

Figures 14 - 16 contain flow field images for the vehicle rolled to $\beta = -10°$, which causes the starboard nozzle axes to aim directly into the oncoming freestream. The starboard plumes are deflected upward by the scarfed nozzle exits and elevated pressure between the plume banks, but they are closer to flowing directly into the freestream than any other cases considered. This case was initially selected because this jet orientation tends to amplify the effects of the floating stagnation point instability, which should make this a challenging test of simulation accuracy. None of the present CFD options performed well, as shown in the comparisons of heatshield C_p in Fig. 14.

Differences in the bow shock shapes are the dominant cause of differences in heatshield loads between CFD and experiment. The experimental Schlieren images in Fig. 15 are subjectively representative of the range of bow-shock shapes seen in the video of this flow. The visible bow shock ahead of the vehicle tends to be within 15° of normal to the

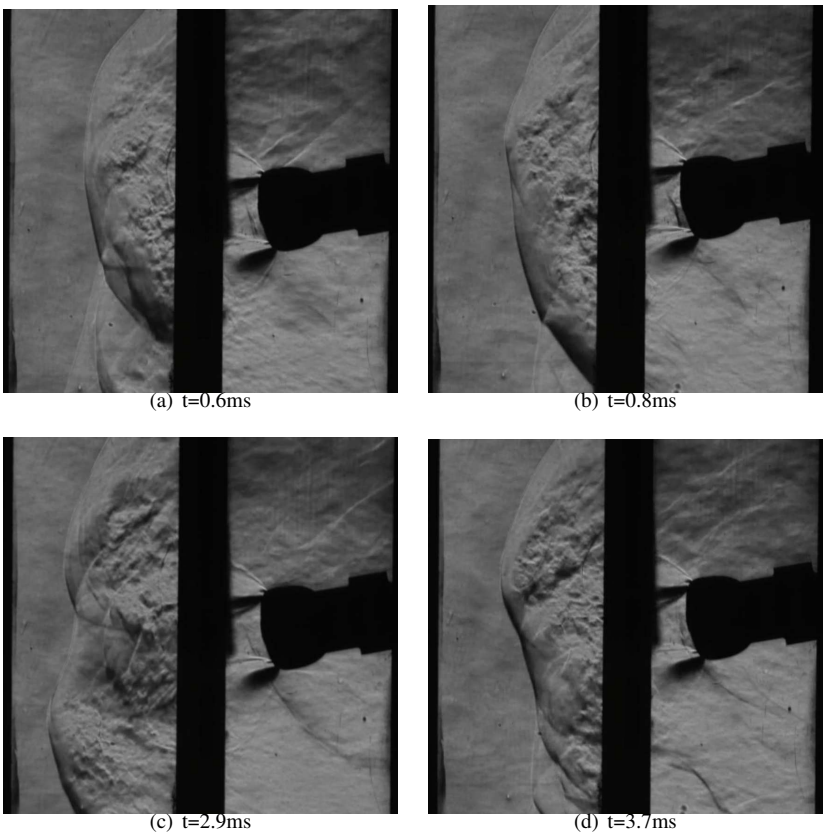

(a) t=0.6ms (b) t=0.8ms

(c) t=2.9ms (d) t=3.7ms

Fig. 15 Instantaneous Schlieren images from Edquist[20], selected to be exhibit range of bow-shock shape, at $M = 2.4, CT = 2.5\phi = 90°, \beta = 10°$. (Schlieren images were recorded at $\beta = 10°$ and mirrored to $\beta = -10°$, to match CFD and experimental PSP measurement conditions.)

freestream. Figure 16 gives plots of C_{p0} for the time-averaged TMRC and DES solutions on the $y = 0$ centerplane of the vehicle, between the inner-most nozzles. The central region of bow shock in CFD has a broad 'V' shape with oblique shocks between the upper and lower plumes that are $\sim 45°$ from normal to the freestream at their steepest point. There is a second oblique shock emanating from the point of the V in both C_{p0} images. The contour plots of C_{p0} show losses across these shocks, but these losses are much less than if the shocks were nearly normal. This stream of elevated C_{p0} flows along a serpentine path between the plume banks to the heatshield, where it causes the 'arcs' of elevated C_p in all CFD solutions in Fig. 14. While there are many differences between the Schlieren and CFD visualization methods, it is reasonable to believe that the bow shock shapes differ significantly, with higher shock-losses across the experiment's bow shock.

There are also differences in losses (and gains) of C_{p0} along the serpentine path that flows to the heatshield. The DES solution has about a $\Delta C_{p0} \sim 0.6$ greater loss than TMRC along this path. Figure 14 also shows that the TMRC solution has $\Delta C_p \sim 0.6$ higher pressure in the high-pressure arc on the heatshield. The DES solution also exhibits a small rise in C_{p0} at the heatshield as *tke* is converted to mean pressure where it impinges on the heatshield. This is an example of the *tke's* omission from CFD's mean energy equation, and the definition of C_{p0} used here, leading to observable irregularities in flow behavior. Typically, C_{p0} should remain constant along a streamline in this steady averaged flow, or decrease by known dissipative mechanisms.

The modeled and total (modeled + resolved) *tke* are given in Fig. 16 (c-f). The modeled *tke* is substantially different in TMRC and DES solutions, as expected, while the total *tke* is reasonably similar in many regions. The total *tke* in the V region of the bow shock results from fluctuations of the bow shock position, not from 'true' *tke* associated with vorticity fluctuations. Note the rapid decay of this non-vortical turbulence behind the upper leg of the V region of the bow shock, and the more persistent vortical *tke* behind the point of the V. This is an example of how shocks may, or may not, generate turbulence. There are two notable regions where DES predicts significantly higher total *tke* than

TMRC SST DES

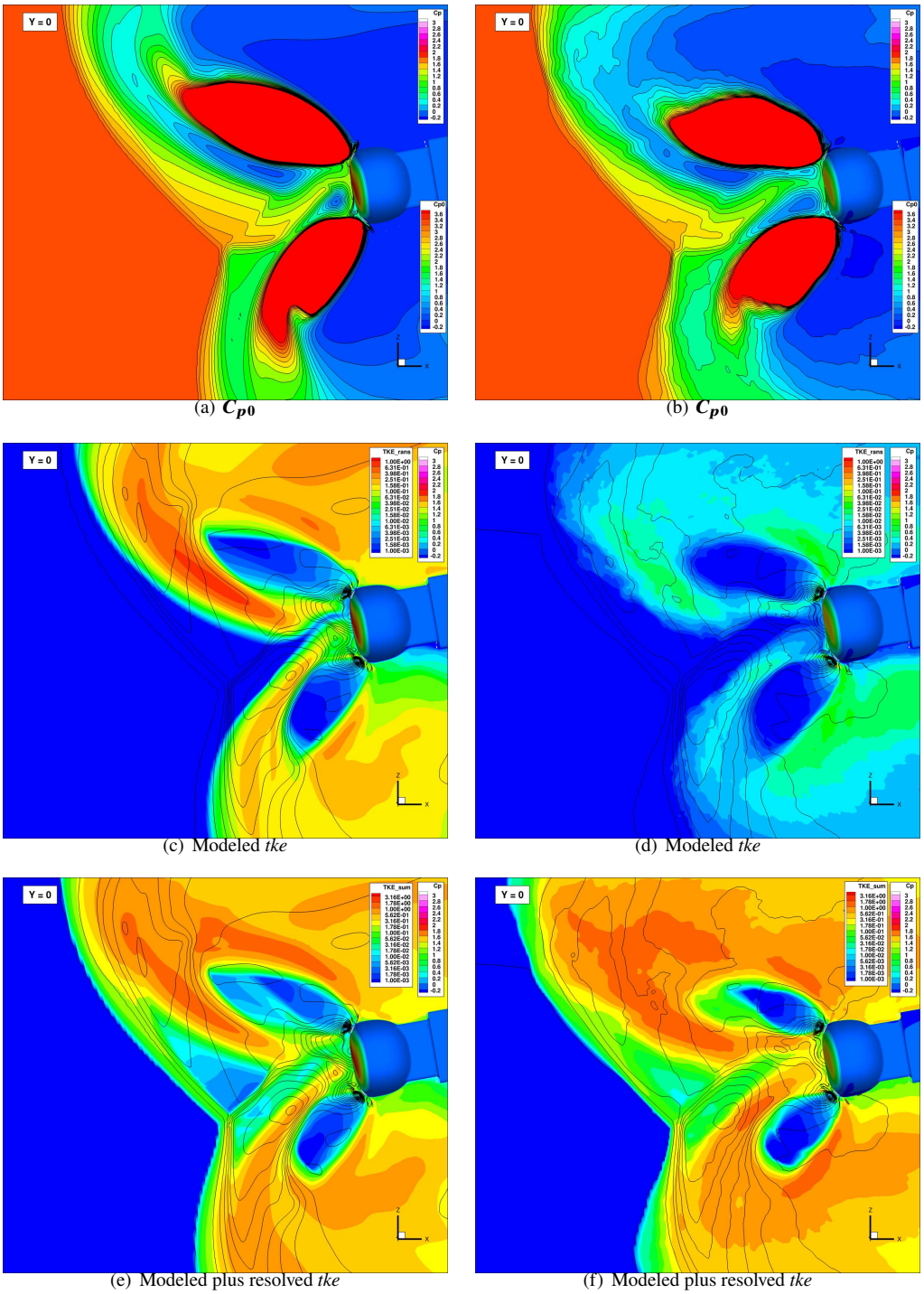

(a) C_{p0} (b) C_{p0}

(c) Modeled *tke* (d) Modeled *tke*

(e) Modeled plus resolved *tke* (f) Modeled plus resolved *tke*

Fig. 16 Time-averaged solutions from TMRC and SST-DES at $M = 2.4, CT = 2.5$, $\phi = 90°$, $\beta = -10°$. Color contours on the $y = 0$ centerline plane are stagnation pressure coefficient C_{p0}, the modeled *tke* from the *k-ω* model and the sum of modeled and resolved *tke* (note the different contour levels); black contour lines in (c-f) are C_p, as a reference for flow structure. C_p color contours are given on the model's surface.

TMRC. (1) Turbulence at the ends of the plume banks (red in the C_{p0} figure) typically involves very dynamical 'plume termination' shocks, where the flow can drop to subsonic. RANS models are unlikely to predict this region well. (2) The inner plume shear layers of both upper and lower plume-banks are thicker and with higher total *tke* in the DES solution. DES is resolving higher *tke* than the TMRC model predicts, for an RC-unstable high-speed shear layer, which is the type of flow the TMRC model has predicted well in the mixing layers and LAV plumes. Furthermore, the initial plume shear layers are thin, and DES is not being run with fine-enough resolution to capture turbulence in that region with good accuracy. Objectively, DES is expected to underpredict *tke* in these shear layers.

There is an additional hint at the nature of the aerodynamics, in the experimental results of Edquist[20], for the HIAD 1A configuration which has a nozzle splay angle of zero. As with some of the plumes on the CobraMRV rolled to $\beta = 10°$, its jets point directly into the oncoming freestream when it operates at $\alpha = 0°$. The revealing measurement is C_p at the center of the heatshield for $M = 2.386$ and $\alpha = 0°$, which is $C_p \sim 1.7$ for $CT \leq 2.0$, and $C_p \sim 0.1$ for $CT \geq 2.0$. At $CT = 2.0$ repeat runs gave $C_p \sim 1.7$ or 0.0; it exhibits a strongly non-unique behavior. There is also a trend for the 1A configuration to experience a sharp drop in this C_p with increasing CT when all 8 jets were powered, and a smooth decrease in C_p with increasing CT when the full CT was achieved with only 4 jets powered. This non-linear response to CT may be explained by entrainment by the jets, of the flow between the jets, and the aerodynamic splaying of the jets by elevated pressure between the jets, in combination with the shock-loss mechanisms described previously. When that entrainment is high enough, the jets tend to 'stick together', to create a uniform back-pressure and strong shock normal to the freestream. The Schlieren images for the CobraMRC at $\beta = 10°$ suggest that the jets expand very rapidly, which is needed to provide a broad area of back pressure to support the more nearly normal bow shock. When the entrainment is reduced, the jets are splayed, which leads to a non-uniform back pressure, oblique regions of the bow shock and higher pressure between the jets with a further increase in the aerodynamic splaying of the jets. The measurements for HIAD 1A configuration suggest that the proposed behavior is bi-stable.

The proposed scenario suggests that entrainment into the jets near the heatshield is a critical variable factor that governs the overall flow's behavior. The TMRC model has displayed resonable accuracy for the barrel-shaped plume shear layers in the aerodynamically quiet environment of the pellet problem, so something about this configuration degrades its accuracy. A likely mechanism is that turbulence from the plumes flows back to the heatshield and energizes the initial plume shear layers. The nozzle lip is the point of maximum receptivity to a noisy environment. The sensitivity and accuracy of RANS models to this receptivity in a noisy environment is expected to be poor. DES certainly has the potential to resolve this mechanism, but there is a high computational cost to resolve turbulence in the very thin initial plume shear layers. Under flight conditions for which this proposed mechanism is critical, RANS modeling should be expected to give poor accuracy, and the high resolution required for DES to perform well has not been achieved in the present work.

V. Summary & Conclusions

This report describes a turbulence model named TMRC for its key elements. A second-order temporal Taylor series analysis leads to equations for the turbulent mass-flux vector and momentum-flux tensor, as functions of time, which leads to model predictions of the equilibrium values of these fluxes. This is an algebraic stress model (ASM) with similarities to the QCR model[13]. The Taylor series predicts that the eddy-viscosity stress is *the* correct first-order model of the stress tensor. The second-order terms lead to the ASM part of the model. Among the second-order terms: are a rotation of the stress tensor similar to the QCR model, a history term due to the $\dot{S}_{ij}$ term commonly used in the SA model[23], and a turbulence generation mechanism consistent with Brunt-Väisälä theory. Rotation and curvature (RC) terms naturally decompose into baroclinic and kinematic parts. The other major part of the model involves terms for classical compressibility (CC) effects that reduce turbulence at elevated convective Mach number M_c, and how the strength of the CC model is reduced in the presence of destabilizing RC effects. The model is tuned on LES data for mixing layers over a wide range of M_c and RC effects. The LES results demonstrate that destabilizing RC effects cause a reduction of CC effects, which the TMRC model mimics with reasonable accuracy. Previously published modifications of the SST model for RC, CC and ASM-related effects fail to predict most trends observed in the LES data from mixing layers subject to combined RC and CC effects. An important property of TMRC is that its versions of the RC, CC and ASM modeling are always enabled, and they function well together. In contrast, the simultaneous use of the CC, RC and QCR model options currently available in Overflow (and presumably many other CFD solvers) gives grossly distorted rocket motor plumes on the Orion launch abort vehicle. The TMRC model is an extension of the standard k-ω-SST model.

The application of the TMRC model to supersonic retro-propulsion on the CobraMRV Mars-lander concept vehicle has given mixed results. In the companion paper by Matsuno[8], the TMRC model is competitive with DES in terms of accuracy and can be used on a coarser grid than needed for DES. The single CobraMRV case studied in this paper involves the vehicle rolled by 10° so one bank of jet nozzles is directed straight into the freestream. While all turbulence model options, stock SST, TMRC and DES, give very poor results, the DES results were clearly superior to the TMRC results. Possible mechanisms that lead to this outcome are discussed. A likely cause is that highly turbulent flow from the exhaust jets impinges back onto the heatshield near the nozzles, which increases turbulence in the initial jet shears, and further interacts with large-scale features of the jets. DES with sufficient resolution should be capable of predicting this behavior, but RANS modeling is likely incapable of predicting the core physical processes of this behavior.

Acknowledgements

Support for this work came from several sources. The model development work was supported by the NASA Engineering and Safty Center, NESC, and the Computational Aerosciences Project within the Orion Program. The simulations of the CobraMRV vehicle were supported by Aerosciences Evaluation and Test Capabilities, AETC, portfolio office. Computations were performed on the NAS facility at the NASA Ames Research Center. Special thanks to colleagues in the Ames Research Center, Systems Analysis Office.

References

[1] Menter, F. R., "Two-equation eddy-viscosity turbulence models for engineering applications," *AIAA journal*, Vol. 32, No. 8, 1994, pp. 1598–1605.

[2] Menter, F. R., Kuntz, M., Langtry, R., et al., "Ten years of industrial experience with the SST turbulence model," *Turbulence, heat and mass transfer*, Vol. 4, No. 1, 2003, pp. 625–632.

[3] Suzen, Y., Hoffmann, K., and Forsythe, J., "Application of several turbulence models for high speed shear layer flows," *37th Aerospace Sciences Meeting and Exhibit*, 1999, p. 933.

[4] Shur, M. L., Strelets, M. K., Travin, A. K., and Spalart, P. R., "Turbulence modeling in rotating and curved channels: assessing the Spalart-Shur correction," *AIAA journal*, Vol. 38, No. 5, 2000, pp. 784–792.

[5] Smirnov, P. E., and Menter, F. R., "Sensitization of the SST turbulence model to rotation and curvature by applying the Spalart-Shur correction term," *Turbo Expo: Power for Land, Sea, and Air*, Vol. 43161, 2008, pp. 2305–2314.

[6] Childs, R., Garcia, J., Melton, J., Rogers, S., Shestopolov, A., and Vicker, D., "Overflow Simulation Guidelines for Orion Launch Abort Vehicle Aerodynamic Analyses," *29th AIAA Applied Aerodynamics Conference*, 2011, p. 3163.

[7] Edquist, K., Glass, C., Korzun, A., Wood, W., West, T., Alter, S., Canabal, F., Childs, R., Halstrom, L., and Matsuno, K., "Computational Analysis of Two Mars Powered Descent Vehicle Concepts Tested in the Langley Unitary Plan Wind Tunnel," *AIAA Aviation Forum 2024*, 2024, pp. –.

[8] Matsuno, K., "Comparison of OVERFLOW Computational and Experimental Results of the CobraMRV Mars Entry Vehicle Concept during Supersonic Retropropulsion (submitted)," *AIAA Aviation Forum 2024*, 2024, pp. –.

[9] Halstrom, L., "Comparison of OVERFLOW Computational and Experimental Results for a Blunt Mars Entry Vehicle Concept During Supersonic Retropropulsion (submitted)," *AIAA Aviation Forum 2024*, 2024, pp. –.

[10] Saffman, P. G., "Development of a Complete Model for the calculation of Turbulent Shear Flows," *Chapter II of Statistical mechanics and Dynamical Systems by David Ruelle and papers from the 1976 Duke Turbulence Conference, Duke University Mathematics Series III*, 1976, pp. –.

[11] Knight, D., and Saffman, P., "Turbulence model predictions for flows with significant mean streamline curvature," *16th Aerospace Sciences Meeting*, 1978, p. 258.

[12] Wilcox, D., and Rubesin, M., "Progress in turbulence modelling for complex flow fields including effects of compressibility," Tech. rep., NASA, 1980.

[13] Mani, M., Babcock, D., Winkler, C., and Spalart, P., "Predictions of a supersonic turbulent flow in a square duct," *51st AIAA Aerospace Sciences Meeting Including the New Horizons Forum and Aerospace Exposition*, 2013, p. 860.

[14] Rumsey, C., "https://turbmodels.larc.nasa.gov/," , 2023.

[15] Wilcox, D. C., "Formulation of the k-ω turbulence model revisited," *AIAA journal*, Vol. 46, No. 11, 2008, pp. 2823–2838.

[16] Slessor, M., Zhuang, M., and Dimotakis, P., "Turbulent shear-layer mixing: growth-rate compressibility scaling," *Journal of Fluid Mechanics*, Vol. 414, 2000, pp. 35–45.

[17] Matsuno, K. V., *Compressibility Variable Density and Curvature Effects on Turbulent Shear Layers*, Stanford University, 2022.

[18] Rossmann, T., "An experimental investigation of high-compressibility mixing layers," Ph.D. thesis, Stanford University, 2002.

[19] Rossmann, T., Mungal, M. G., and Hanson, R. K., "Evolution and growth of large-scale structures in high compressibility mixing layers," *Journal of Turbulence*, Vol. 3, No. 1, 2002, p. 009.

[20] Edquist, K., "Testing of Two Mars Powered Descent Lander Vehicle Concepts in the Langley Unitary Plan Wind Tunnel," *AIAA Aviation Forum 2024*, 2024, pp. –.

[21] Edquist, K. T., Korzun, A. M., Kleb, W. L., Hawke, V., Rizk, Y. M., Olsen, M. E., and Canabal, F., "Model Design and Pre-Test CFD Analysis for a Supersonic Retropropulsion Wind Tunnel Test," *AIAA Scitech 2020 Forum*, 2020, p. 2230.

[22] Edquist, K. T., "Status of mars retropropulsion testing in the langley unitary plan wind tunnel," *AIAA Scitech 2022 Forum*, 2022, p. 0911.

[23] Spalart, P., and Allmaras, S., "A one-equation turbulence model for aerodynamic flows," *30th aerospace sciences meeting and exhibit*, 1992, p. 439.